



**HAL**  
open science

## Validation of metaxin-2 deficient *C. elegans* as a model for MandibuloAcral Dysplasia associated to mtX-2 (MADaM) syndrome

Chloé Talarmin-Gas, Georges Smolyakov, Cleo Parisi, Cyril Scandola, Valérie Andrianasolonirina, Cloé Lecoq, Valentine Houtart, Song-Hua Lee, Homa Adle-Biassette, Bénédicte Thiébot, et al.

### ► To cite this version:

Chloé Talarmin-Gas, Georges Smolyakov, Cleo Parisi, Cyril Scandola, Valérie Andrianasolonirina, et al.. Validation of metaxin-2 deficient *C. elegans* as a model for MandibuloAcral Dysplasia associated to mtX-2 (MADaM) syndrome. *Communications Biology*, 2024, 7 (1), pp.1398. 10.1038/s42003-024-06967-z . hal-04829679

**HAL Id: hal-04829679**

**<https://hal.science/hal-04829679v1>**

Submitted on 10 Dec 2024

**HAL** is a multi-disciplinary open access archive for the deposit and dissemination of scientific research documents, whether they are published or not. The documents may come from teaching and research institutions in France or abroad, or from public or private research centers.

L'archive ouverte pluridisciplinaire **HAL**, est destinée au dépôt et à la diffusion de documents scientifiques de niveau recherche, publiés ou non, émanant des établissements d'enseignement et de recherche français ou étrangers, des laboratoires publics ou privés.



Distributed under a Creative Commons Attribution - NonCommercial - NoDerivatives 4.0 International License

<https://doi.org/10.1038/s42003-024-06967-z>

# Validation of metaxin-2 deficient *C. elegans* as a model for MandibuloAcral Dysplasia associated to *mtx-2* (MADaM) syndrome



Chloé Talarmin-Gas<sup>1,2</sup>✉, Georges Smolyakov<sup>1,2</sup>, Cleo Parisi<sup>1,2</sup>, Cyril Scandola<sup>3</sup>, Valérie Andrianasolonirina<sup>1,2</sup>, Cloé Lecoq<sup>1,2</sup>, Valentine Houtart<sup>2</sup>, Song-Hua Lee<sup>4</sup>, Homa Adle-Biassette<sup>1,2,5</sup>, Bénédicte Thiébot<sup>6</sup>, Timothy Ganderton<sup>1,2</sup> & Philippe Manivet<sup>1,2,4</sup>✉

MandibuloAcral Dysplasia associated to MTX2 gene (MADaM) is a recently described progeroid syndrome (accelerated aging disease) whose clinical manifestations include skin abnormalities, growth retardation, and cardiovascular diseases. We previously proposed that *mtx-2*-deficient *C. elegans* could be used as a model for MADaM and to support this, we present here our comprehensive phenotypic characterization of these worms using atomic force microscopy (AFM), transcriptomic, and oxygen consumption rate analyses. AFM analysis showed that young *mtx-2*-less worms had a significantly rougher, less elastic cuticle which becomes significantly rougher and less elastic as they age, and abnormal mitochondrial morphology. *mtx-2* *C. elegans* displayed slightly delayed development, decreased pharyngeal pumping, significantly reduced mitochondrial respiratory capacities, and transcriptomic analysis identified perturbations in the aging, TOR, and WNT-signaling pathways. The phenotypic characteristics of *mtx-2* worms shown here are analogous to many of the human clinical presentations of MADaM and we believe this validates their use as a model which will allow us to uncover the molecular details of the disease and develop new therapeutics and treatments.

Progeroid syndromes are a small group of rare genetic diseases including Hutchinson-Gilford Progeria<sup>1</sup> (HGPS), Mandibuloacral Dysplasia<sup>2</sup> (MAD) and Werner syndrome<sup>3</sup> (WS), which are commonly referred to as accelerated aging disorders. Despite being caused by different gene mutations, they share similar clinical features including cardiovascular diseases, osteoporosis, skin alterations and growth retardation. Clinical signs manifest early in life and patients have a reduced lifespan, rarely living beyond their 20s<sup>4</sup>. We, and others, recently reported on a novel progeroid syndrome called MADaM<sup>5,6</sup> (Mandibuloacral dysplasia associated to MTX2), which has clinical features resembling HGPS<sup>7,8</sup> and is caused by recessive homozygous null mutations in MTX2, a gene that encodes the outer mitochondrial membrane (OMM) protein Metaxin-2 (MTX2) (Uniprot O75431<sup>9</sup>).

MTX2, through direct interaction with its partner Metaxin-1 (MTX1), faces the cytosolic compartment<sup>10,11</sup> and while its exact functions are yet to be described, both have been shown to be involved in protein translocation into mitochondria<sup>10</sup> as part of the mitochondrial sorting and assembly machinery (SAM) responsible for the correct integration of  $\beta$ -barrel proteins into the OMM<sup>11,12</sup>. SAM is responsible for protein trafficking into the mitochondrial membrane and is involved in Bak activation during TNF $\alpha$ -induced apoptosis. The MICOS complex (mitochondrial contact site and cristae organizing system) is associated with SAM and is partly anchored in the inner mitochondrial membrane (IMM). It is crucial for the formation and maintenance of cristae structure on which mitochondrial function depends<sup>13,14</sup>. In MADaM patient-derived fibroblasts, loss of MTX1 and MTX2 causes mitochondrial network fragmentation, decreased oxidative

<sup>1</sup>Université Paris Cité, INSERM UMR 1141 "NeuroDiderot", FHU Iio2-D2, Paris, France. <sup>2</sup>AP-HP, DMU BioGem, Centre de Ressources Biologiques Biobank Lariboisière/Saint Louis (BB-0033-00064), Hôpital Lariboisière, Paris, France. <sup>3</sup>Institut Pasteur, Université Paris Cité, Ultrastructural Bioimaging Unit, 75015 Paris, France. <sup>4</sup>CeleScreen SAS, Paris, France. <sup>5</sup>AP-HP, DMU DREAM, Service d'Anatomocytopathologie, Hôpital Lariboisière, Paris, France. <sup>6</sup>CY Cergy Paris Université, Université d'Evry, Université Paris-Saclay, CNRS, LAMBE, F-95000 Cergy, France. ✉e-mail: [chloejosephine.talarmin@aphp.fr](mailto:chloejosephine.talarmin@aphp.fr); [philippe.manivet@aphp.fr](mailto:philippe.manivet@aphp.fr)

phosphorylation (OxPhos), resistance to TNF- $\alpha$  induced apoptosis, increased senescence and autophagy, and reduced proliferation<sup>5</sup>. Our previous observations of *mtx-2* k.o. *Caenorhabditis elegans* (*mtx-2 C. elegans*) mirrored some of these patient-derived cell line characteristics and we described alterations in the mitochondrial network, abnormal mitochondria morphology, significant developmental delay, and reduced fertility<sup>5</sup>. We proposed that *mtx-2 C. elegans* could be a model for MADaM, but that additional work was needed to properly validate it, in particular, to show that the phenotypic effects of a loss of MTX2 were analogous to the clinical presentations.

As a model organism, *C. elegans* has been used to study a range of diseases including; neurodegenerative disorders such as Alzheimer's disease<sup>15,16</sup>, laminopathies including HGPS<sup>17,18</sup> and WS<sup>19</sup>, Amyotrophic lateral sclerosis<sup>20,21</sup> (ALS), and Parkinson's disease (PD), where cumulative evidence suggests that mitochondrial dysfunction plays a role in disease pathology<sup>22</sup>. They have been used to study the contribution of metaxins to mitochondrial transport in *C. elegans* neurons<sup>23</sup> and the physiological aging process<sup>24,25</sup>, and have also proven to be an excellent tool for researchers wanting to investigate mitochondria and complex mitochondrial-related processes which can be challenging to study in higher organisms. Mitochondrial dynamics in *C. elegans* are intimately linked to mitochondrial morphology and structure, tissue function, and lifespan<sup>24</sup>. The *C. elegans* cuticle has been touted as a model for human skin<sup>26,27</sup> with vast potential as a drug testing system for use in the pharmaceutical and cosmetic industries.

Here, we present our comprehensive characterization of *mtx-2 C. elegans* using Atomic Force Microscopy (AFM), transcriptomics, Oxygen Consumption Rate (OCR), Scanning Electron Microscopy (SEM), and phenotype analysis. In addition to *mtx-2 C. elegans*, we have also briefly characterized a worm strain with a loss of general anesthetic sensitivity 1 (*gas-1 C. elegans*). It has been shown that loss of *gas-1* in worms significantly disrupts normal mitochondrial function (in particular Complex I-dependent respiration) without any visible effects on their morphology<sup>28</sup>, and thus provides us with an interesting comparison strain for this study.

## Results

### Individual mitochondria are significantly elongated and more likely to be asymmetrical in *mtx-2* worms

We previously showed that loss of *mtx-2* in both human cells and worms was associated with a fragmented mitochondrial network and an increase in mitochondria with abnormal morphology<sup>5</sup>. To examine this in greater detail, we used AFM to analyze the size, shape, and mechanical behavior of individual mitochondria from L4 stage wild type N2 (WT), *mtx-2*, and *gas-1* worms. Although AFM has previously been used to study individual mitochondria<sup>29,30</sup>, this is, to the best of our knowledge, the first study to examine mitochondria from *C. elegans*. We found that mitochondria extracted from WT worms displayed regular, rounded shapes (Fig. 1a) with a height of  $177 \pm 118$  nm, while those from *mtx-2* worms appeared more spread out with a height of  $272 \pm 190$  nm, and an irregular membrane surface (Fig. 1b). Mitochondria from *gas-1* worms also displayed some topographic irregularities (Fig. 1c) with a height of  $229 \pm 150$  nm. Mitochondria from *mtx-2* worms were significantly elongated (Fig. 1d,  $798 \pm 268$  nm) compared to WT ( $600 \pm 245$  nm,  $p = 0.0058$ ) and *gas-1* derived mitochondria ( $573 \pm 138$  nm,  $p = 0.0109$ ) and no statistically significant differences were found between strains in terms of height and width (Fig. 1d). A complete statistical analysis of morphological characteristics at L4 can be found in Supplementary Table 1. An analysis of mitochondrial shape discriminating between symmetrical (proper round, aspect ratio < 1.2 and proper oval, aspect ratio  $\geq 1.2$ ), and asymmetrical shapes (characteristic examples can be found in Supplementary Fig. 1) showed us that mitochondria in *mtx-2* and *gas-1* strains were mostly asymmetrical (proper round: 0% and 10%, proper oval: 24% and 14%, and asymmetrical: 76% and 76%, respectively), whereas WT mitochondria were mostly symmetrical (proper round: 50%, proper oval: 41%, and asymmetrical: 9%). We see that the loss of *mtx-2* affects both size and shape of mitochondria, while the loss of *gas-1* only affects shape. No statistically significant differences were

observed in the elastic modulus E (a *de facto* measurement of organelle flexibility/stiffness) between mitochondria of the 3 worm strains ( $0.80 \pm 0.75$  MPa,  $0.75 \pm 0.90$  MPa, and  $0.77 \pm 0.77$  MPa, for WT, *mtx-2*, and *gas-1* respectively, Fig. 1d).

### Mitochondrial asymmetry and stiffness increases with age in WT and *mtx-2 C. elegans*

We also compared size, shape, and mechanical behavior of WT, *mtx-2*, and *gas-1* mitochondria at different ages; late larval stage (L4), reproductive (D2), and post-reproductive period (D8). Compared to L4 WT mitochondria, D2 and D8 had significantly reduced height ( $96 \pm 50$  nm,  $p = 0.0021$  and  $83 \pm 36$  nm,  $p = 0.0002$ , respectively), length ( $386 \pm 129$  nm,  $p = 0.0021$  and  $423 \pm 149$  nm,  $p = 0.0136$ ), and width ( $316 \pm 100$  nm,  $p = 0.0019$  and  $298 \pm 86$  nm,  $p = 0.0002$ , respectively) (Fig. 1e) and the proportion of irregularly shaped WT mitochondria increased with age; L4 - proper round: 50%, proper oval: 41%, and asymmetrical: 9%, D2 - proper round: 36%, proper oval: 36%, and asymmetrical: 28%, and D8 - proper round: 14%, proper oval: 18%, and asymmetrical: 68%.

Similar results were seen in *mtx-2* mitochondria; compared to L4, D2 and D8 mitochondria had significantly reduced height ( $85 \pm 65$  nm,  $p = 0.0002$  and  $80 \pm 54$  nm,  $p = 0.0002$ , respectively), length ( $458 \pm 141$  nm,  $p < 0.0001$  and  $524 \pm 138$  nm,  $p = 0.0018$ ) and width ( $380 \pm 143$  nm,  $p = 0.0182$  and  $410 \pm 116$  nm,  $p = 0.1268$ , respectively) (Supplementary Fig. 2). In contrast to WT, irregular mitochondrial shapes were observed at all ages; L4 - proper round: 0%, proper oval: 24%, and asymmetrical: 76%, D2 - proper round: 28%, proper oval: 11%, and asymmetrical: 61%, and D8 - proper round: 16%, proper oval: 5%, and asymmetrical: 79%.

Lastly, *gas-1* mitochondria were also affected by age; compared to L4, D2 mitochondria had significantly lower height ( $103 \pm 57$  nm,  $p = 0.0066$ ), length ( $393 \pm 128$  nm,  $p = 0.0002$ ), and width ( $328 \pm 134$  nm,  $p = 0.0032$ ). D8 mitochondria had significantly lower height than L4 ( $64 \pm 27$  nm,  $p < 0.0001$ ) and D2 mitochondria ( $p = 0.0042$ ), and significantly higher length ( $557 \pm 235$  nm,  $p = 0.0041$ ) and width ( $460 \pm 117$  nm,  $p = 0.0009$ ) than D2 mitochondria (Supplementary Fig. 2). A complete statistical analysis of morphological characteristics of mitochondria at different ages is in Supplementary Table 2. The proportion of irregularly shaped *gas-1* mitochondria decreased with age, in favor of proper round shape; L4 - proper round: 10%, proper oval: 14%, and asymmetrical: 76%, D2 - proper round: 50%, proper oval: 28%, and asymmetrical: 22%, and D8 - proper round: 62%, proper oval: 5%, and asymmetrical: 33%.

No statistically significant differences were observed in mitochondrial size between worm strains at D2. However, at D8, *mtx-2* and *gas-1* mitochondria were significantly longer ( $p = 0.0309$  and  $p = 0.0161$ , respectively) and wider ( $p = 0.0022$  and  $p < 0.0001$ , respectively) compared to WT, and *gas-1* mitochondria had significantly lower height ( $p = 0.028$ ) (Supplementary Fig. 2). A complete statistical analysis of morphological characteristics at D2 and D8 can be found in Supplementary Table 1. In terms of shape, at D2, *mtx-2* mitochondria were mostly asymmetrical (61%) compared to WT (28%) and *gas-1* (22%) mitochondria, whereas at D8, WT and *mtx-2* were mostly asymmetrical (68% and 79%, respectively) compared to *gas-1* (33%). In terms of mechanical behavior, in all strains, the elastic modulus of D2 and D8 mitochondria was mostly significantly higher than L4 (WT:  $0.80 \pm 0.75$  MPa vs  $4.42 \pm 5.06$  MPa,  $p = 0.0018$  and  $5.65 \pm 2.62$  MPa,  $p < 0.0001$ , (Fig. 1e), *mtx-2*:  $0.75 \pm 0.90$  MPa vs  $2.67 \pm 2.38$  MPa,  $p = 0.0019$  and  $3.67 \pm 3.44$  MPa,  $p = 0.0002$ , and *gas-1*:  $0.77 \pm 0.77$  MPa vs  $2.28 \pm 3.02$  MPa,  $p = 0.0759$  and  $5.42 \pm 3.11$  MPa,  $p < 0.0001$ , Supplementary Fig. 2), showing that mitochondrial stiffness increases with age.

No statistically significant differences were observed in the E between mitochondria of the 3 worm strains at D2 and D8 (Supplementary Fig. 2).

### Basal and maximal respiration are reduced in *mtx-2* worms

We previously showed that MADaM patient-derived cells had lower expression of respiratory complex proteins and a reduction in respiration dedicated to ATP synthesis and basal routine respiration, all evidence of a

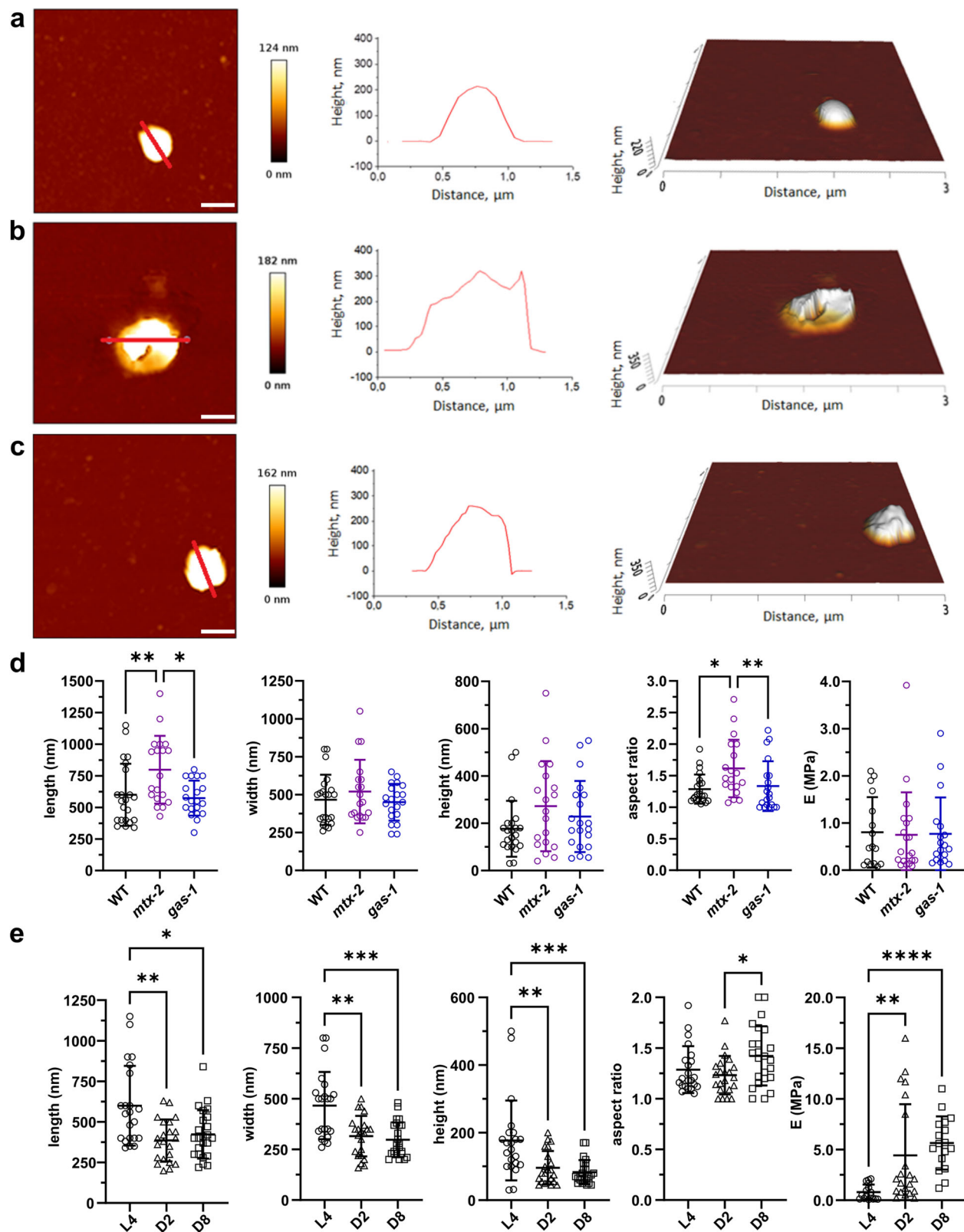


**Fig. 1 | Characterization of morphology and mechanical properties of individual mitochondria by AFM.** From left to right: representative 2D topography image of the mitochondrial surface (scale bar 500 nm), height profile performed along the red line of the 2D topography image, and corresponding 3D topography image for L4 stage **a** WT, **b** *mtx-2*, and **c** *gas-1* worms. Scatter plots (mean  $\pm$  SD) of (from left to right) length, width, height, aspect ratio, and elastic modulus (E) of mitochondria

extracted from **d** the 3 worm strains at L4 stage (length, width, height, and aspect ratio: WT  $n = 22$ , *mtx-2*  $n = 19$ , *gas-1*  $n = 20$ ; Elastic modulus: WT  $n = 16$ , *mtx-2*  $n = 20$ , *gas-1*  $n = 18$ ) and **e** WT worms at L4 stage, D2, and D8 of adulthood (length, width, height, and aspect ratio: D2  $n = 22$ , D8  $n = 24$ ; Elastic modulus: D2  $n = 21$ , D8  $n = 17$ ). Statistically significant differences are shown (\* $p < 0.05$ , \*\* $p < 0.01$ , \*\*\* $p < 0.001$ , \*\*\*\* $p < 0.0001$ ).

dysfunctional mitochondrial respiratory chain<sup>5</sup>. To compare the mitochondrial health of WT, *mtx-2*, and *gas-1* worms at D1 of adulthood, we used the Seahorse XFe96 Analyzer to assess oxygen consumption rates (OCR) with carbonyl cyanide-p-trifluoromethoxyphenylhydrazone (FCCP) as a protonophore uncoupler of mitochondrial OxPhos to enable a measurement of the maximal respiratory capacity and the organism's ability to respond to increasing energy demands, and sodium azide as a mitochondrial respiration inhibitor (inhibitor of cytochrome c oxidase, complex IV) to provide a measure of non-mitochondrial respiration<sup>31</sup>.

Basal, maximal, and spare respiration in *mtx-2* worms were all significantly reduced compared to WT worms ( $0.72 \pm 0.27$  vs  $1.51 \pm 0.58$  pmol/min/worm,  $p = 0.0081$ ,  $1.62 \pm 0.49$  vs  $3.04 \pm 1.17$  pmol/min/worm,  $p = 0.0161$ , and  $0.90 \pm 0.25$  vs  $1.53 \pm 0.63$  pmol/min/worm,  $p = 0.0302$ , respectively. Fig. 2b). No other significant differences were observed between either *mtx-2* and *gas-1* or WT and *gas-1* strains, although the reduction in spare respiration between *gas-1* and WT worms was borderline ( $0.92 \pm 0.20$  vs  $1.53 \pm 0.63$  pmol/min/worm,  $p = 0.0579$ ).

Mitochondrial respiratory capacities were significantly reduced in *mtx-2* worms, as shown in the lower basal metabolism, the reduction in energy demand, and spare OCR. The lowered response to FCCP in both *mtx-2* and *gas-1* worms demonstrates a limited ability to adapt to changes in energy requirements which may ultimately affect development, movement, and fertility.

**Extracellular matrix and muscle function genes, and the aging-related and Wnt pathways significantly affected in *mtx-2* worms**

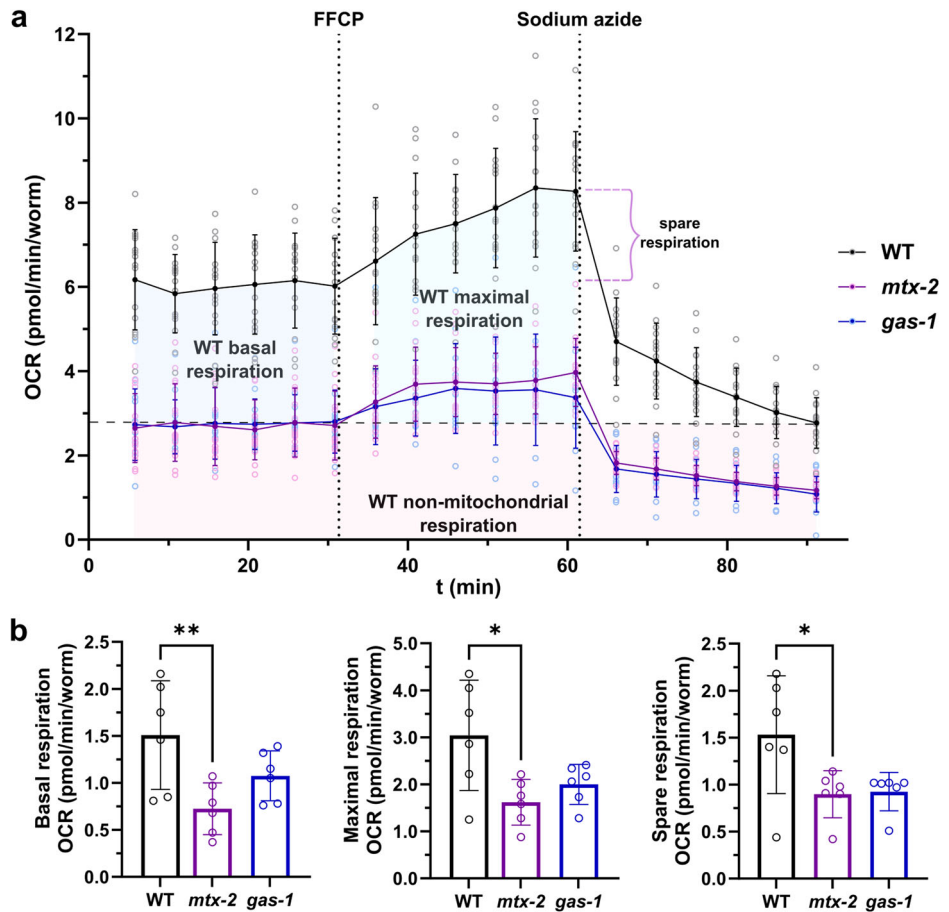
Transcriptomic analysis was performed on total RNA extracted from L4 stage WT and *mtx-2* worms to uncover which genes and functions are affected by loss of *mtx-2*. We found a total of 4294 differentially expressed genes (DEGs) in *mtx-2* worms, 2326 up and 1968 down regulated, with a  $p$  value  $< 0.05$  (Fig. 3b). From this pool, we selected those with a  $\geq \pm 2$ -fold

change in gene expression for further analysis, giving us a final group of 323 DEGs, 315 up and 8 down regulated (Fig. 3a). In the downregulated DEGs, 7/8 were collagen genes (*col-81*, *col-19*, *col-140*, *col-137*, *col-139*, *col-129* and *col-106*) and in total, 106 of the ~170 collagen genes were found in the initial DEG group. Given the importance of collagen genes in cuticle formation and maintenance, this suggests that loss of *mtx-2* may result in morphological and cuticle abnormalities which may be analogous to the skin abnormalities seen in MADaM patients<sup>5</sup>.

When comparing the DEGs to KEGG pathways, we found a large number of DEGs in the aging, TOR and Wnt-signaling pathways in *mtx-2* worms (Supplementary Fig. 3). A full list of DEGs can be found in the Supplementary Data 1, however, a number of genes immediately stood out in our analysis. In the Wnt signaling pathway, *mom-5* (implicated in asymmetric cell division regulation) and *dsh-1* (key switch in wnt signaling) were upregulated and *mig-1* (associated with neuronal migration during development), *lin-17* (associated with certain asymmetric cell division), and *kin-10* (associated with short lifespan phenotype), were downregulated. In the TOR pathway, a number of genes described as “major players”<sup>32</sup> were present in the DEGs; complex components *daf-15*, *let-363*, and *ric-1* were all upregulated, complex interactors T08A11.1, F39C12.1, Y32H12A.8, and F54B3.1 were upregulated and *lmtr-1*, *npp-18*, and *npp-20* were downregulated, and the substrates *atg-13*, *pkc-2*, and *akt-1* and regulators *aak-1* and *daf-18* were all upregulated. Disruptions in the Wnt pathway have been seen in other progeroid syndromes, in particular HGPS.

We used WormCat<sup>33</sup> to identify enriched categories in the final DEGs group because it was specifically designed for analysis of *C. elegans* genomic data and uses a near-complete annotation of the *C. elegans* genome. A full description of the WormCat approach to genomic data sorting and annotation can be found here<sup>33</sup>. Briefly, genes are sorted into nested categories of increasing specificity, initially by physiological function (Category 1), then molecular function (Category 2) or/and cellular location (Category 3). As

**Fig. 2 | Oxygen consumption rate (OCR) of whole worms.** **a** Representative OCR kinetic graph of a single experiment using the 3 worm strains (WT  $n = 15$ , *mtx-2*  $n = 15$ , *gas-1*  $n = 14$ ). The basal, maximal, non-mitochondrial, and spare respiration areas are indicated on the graph for the WT strain. **b** Bar charts (mean  $\pm$  SD) of basal respiration (left), maximal respiration (middle), and spare respiration (right) of three independent experiments ( $n = 6$  measurements). Statistically significant differences are shown ( $*p < 0.05$ ,  $**p < 0.01$ ). FCCPP: carbonyl cyanide-p-trifluoromethoxyphenylhydrazone.



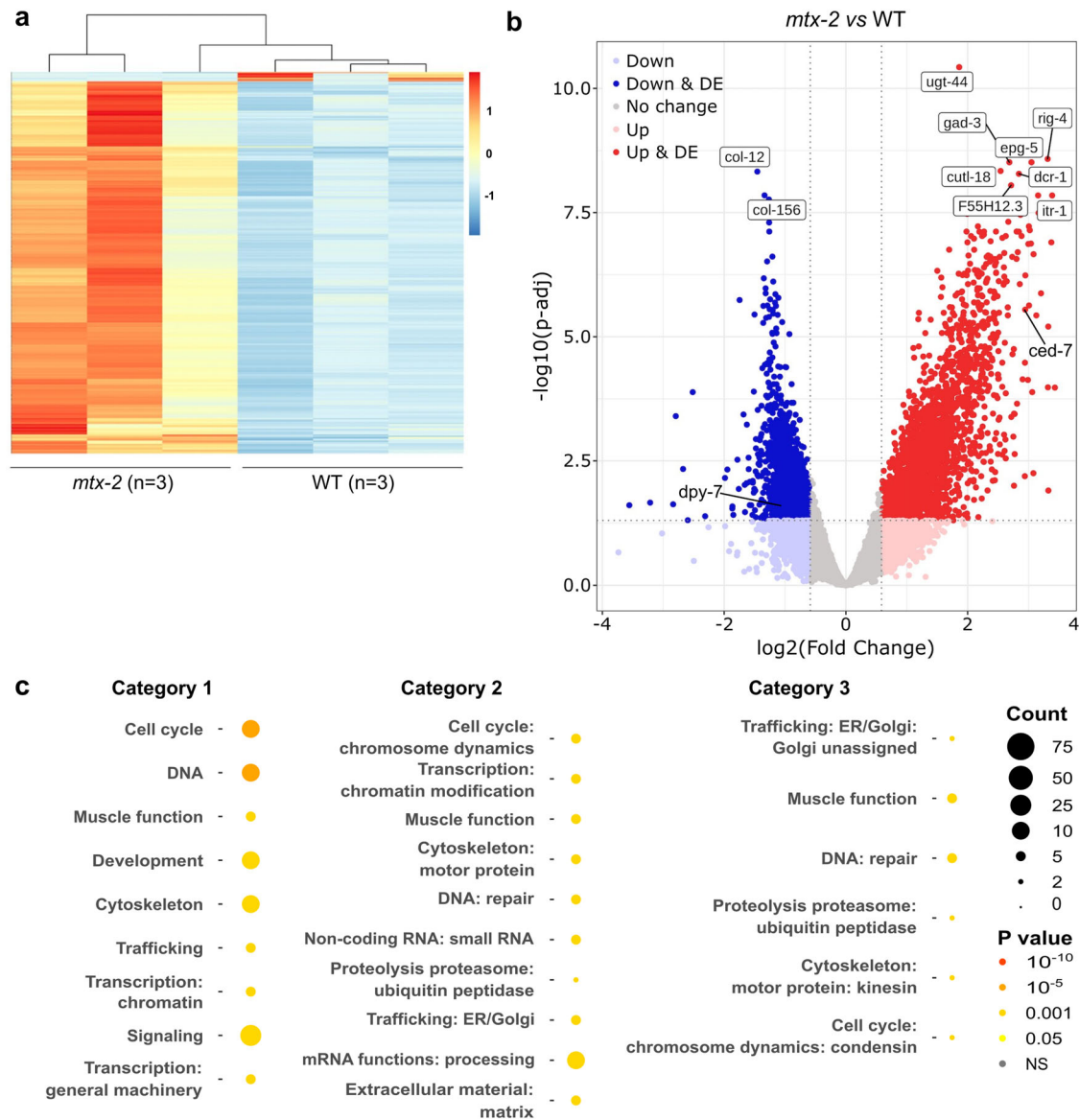


**Fig. 3 | Differentially expressed genes (DEGs) in *mtx-2* worms. a** Heatmap of DEGs ( $n = 323$ ) with  $p$  value adj  $< 0.05$  and  $a \geq 2$ -fold change in expression. **b** Volcano plot of DEGs ( $n = 323$ ). The 10 most statistically significant DEGs and the 2 DEGs further tested by RT-qPCR are indicated on the plot. **c** WormCat

categorisation of final upregulated DEGs ( $n = 315$ ): Category 1 (physiological function), Category 2 (molecular function), Category 3 (cellular location). Circle size indicates number of genes, color indicates  $p$  value.

with traditional GO (Gene Ontology) analyses, genes may be “unassigned/unclassified” which means either their function is not currently known or, in the case of Cat 1 classification, they may be actively involved in more than one physiological function. Of the downregulated DEGs, 7/8 were classified as Extracellular material:Collagen with the other gene Unassigned:Unassigned. In the upregulated DEGs, 73 genes (~22%) were unassigned in Cat 1 and 2, with 42 of those (~13%) completely unassigned. Figure 3c gives a visual summary of the most significantly enriched assigned categories in the upregulated DEGs and full details are in the Supplementary Data 1. The most significantly enriched categories included extracellular matrix (ECM), signaling, cell cycle, and DNA repair. The number of up- and down-regulated ECM DEGs in *mtx-2* worms suggest that the cuticle may be measurably affected by the loss of *mtx-2*, and the prevalence of upregulated cytoskeleton genes may be related to *mtx-2* worm’s abnormal mitochondrial morphology and function<sup>34,35</sup>, as well as the modified mitochondrial organization seen previously<sup>7</sup>. The upregulation of signaling, muscle function, and cell cycle genes may represent an attempt to compensate for the loss of respiratory/energy production capacity in the mitochondria.

We used g:Orth<sup>36</sup> to determine how many genes in the final DEGs group had human orthologs. None of the down-regulated DEGs had any recognized orthologs, but in the up-regulated DEGs, 147/315 (46%) did, with a number of genes having multiple potential orthologs (full details can be found in the Supplementary Data 1). To date, no transcriptomic study of MADaM patients has been done, however, multiple studies have used HGPS<sup>37</sup>, WS<sup>38</sup>, and APS<sup>37</sup> patient-derived samples to perform gene expression profiling. Given the clinical similarities between progeroid syndromes we would expect to see some overlap in genes and cellular processes affected. In those studies, ECM, muscle, DNA repair, and signaling genes were most often found to be affected in those disorders, which is in broad alignment with the findings of this study.

The over-expression of *ugt-44* and *ced-7* and the under-expression of *col-12* and *dpy-7* were confirmed through RT-qPCR (Supplementary Fig. 4). *Ugt-44* and *col-12* were chosen as the two most significantly over- and under-expressed DEGs respectively (Fig. 3b), while *dpy-7* and *ced-7* were chosen because they encode a structural constituent of the collagen- and cuticulin-based cuticle and a key player in apoptosis, respectively<sup>39</sup>.

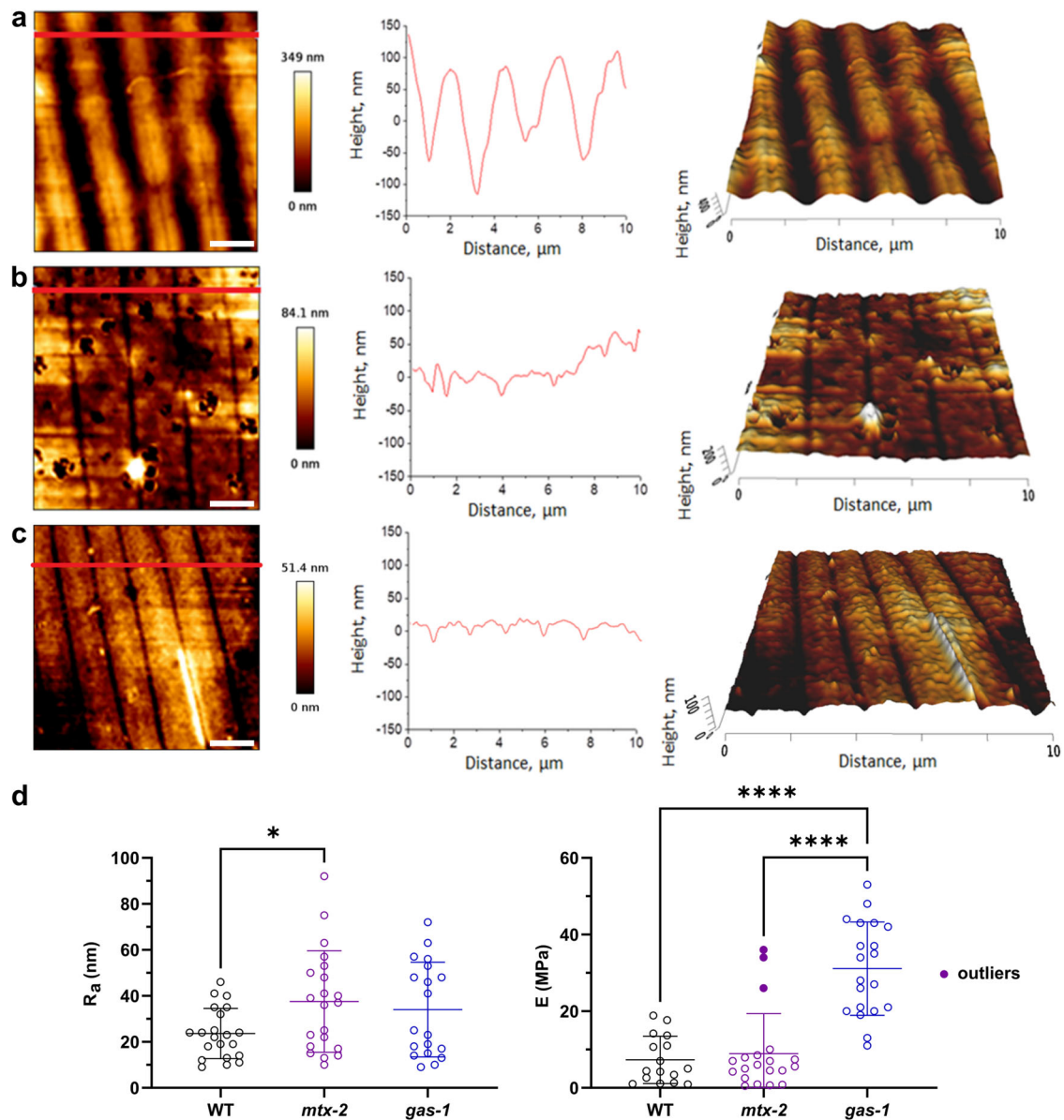


**Fig. 4 | Characterization of cuticle structure and mechanical properties of worms at D2 of adulthood by AFM.** From left to right: representative 2D topography image of a scanned tile of the cuticle surface (scale bar 2  $\mu$ m), height profile performed along the red line of the 2D topography image, and corresponding 3D topography image for **a** WT, **b** *mtx-2*, and **c** *gas-1* worms. **d** Scatter plots (mean  $\pm$  SD) of roughness ( $R_a$ ,

left) and elastic modulus ( $E$ , right) of the 3 worm strains. The  $E$  values for *mtx-2* worms identified as outliers, but not excluded from the analysis, are highlighted ( $R_a$ : WT  $n = 21$ , *mtx-2*  $n = 21$ , *gas-1*  $n = 19$ ;  $E$ : WT  $n = 16$ , *mtx-2*  $n = 20$ , *gas-1*  $n = 20$ ). Statistically significant differences are shown (\* $p < 0.05$ , \*\*\*\* $p < 0.0001$ ).

### Cuticles of *mtx-2* worms significantly rougher than WT at same age

With transcriptomic analysis identifying a wide range of cuticle-related genes affected by a loss of *mtx-2*, we used AFM to examine the cuticle of young and old (D2 and D8 adult) worms in greater detail to assess and quantify any changes.

The cuticle surface of D2 WT worms has a regular structure composed of annuli and furrows (Fig. 4a) whereas in *mtx-2* worms, although annuli and furrows were still observable, the structure was irregular and poorly defined (Fig. 4b). In *gas-1* worms, the structure was regular and closer to WT in appearance, although the annuli and furrows were noticeably shallower (Fig. 4c). Compared to the WT cuticle ( $23.6 \pm 10.9$  nm), the surface roughness ( $R_a$ , Fig. 4d, left) of *mtx-2* was significantly higher ( $37.5 \pm 22.1$  nm,  $p = 0.0441$ ). No statistically significant differences in roughness were seen between *gas-1* ( $34.1 \pm 20.6$  nm) and either WT or *mtx-2*. Our reported  $R_a$  of WT

worms was higher than that described in Essmann et al.<sup>40</sup> which can be explained by their measurement of  $R_a$  being taken directly on the annuli, whereas we measured across the whole AFM height image. No significant difference was seen in the elastic modulus  $E$  (Fig. 4d, right) of *mtx-2* ( $9.0 \pm 10.4$  MPa) and WT worms ( $7.3 \pm 6.2$  MPa), however, the *gas-1* cuticle was significantly stiffer ( $31.1 \pm 12.2$  MPa) than both WT and *mtx-2* ( $p < 0.0001$ ). Outlier  $E$  values for *mtx-2* were identified (Fig. 4d, right), however after performing the analysis with and without the values in question, the level of statistical significance was the same. Thus, these values were considered as true outliers and were not excluded from the dataset. Again, discrepancies are seen between this study and Essmann et al.<sup>40,41</sup>, where their  $E$  of WT worms was lower. This is most likely due to differences in experimental approach; we applied a smaller force on the cuticle which results in a relatively low deformation (the average deformation for WT worms is around 25 nm, while the cuticle thickness is

around 500 nm). Thus, we may consider that only the cuticle contributes to the mechanical response at such low deformation. As the cuticle is stiffer than underlying tissues, the measured elastic modulus is increased.

**Cuticles of *mtx-2* worms become significantly rougher and stiffer with age**

Comparing surfaces of older (Fig. 5a, b, c) and younger cuticles (Fig. 4a, b, c), we see that in all strains, older cuticles display a less regular structure and although the alternation of annuli and furrows was still observable, it is poorly defined. When comparing D8 cuticles, we see that the *mtx-2* roughness ( $R_a$ , Fig. 5d, left) (96.2 ± 64.8 nm) was significantly higher than

both WT ( $25.4 ± 5.8$  nm,  $p = 0.0001$ ) and *gas-1* ( $25.5 ± 13.6$  nm,  $p < 0.0001$ ) and that there was no significant difference between WT and *gas-1* ( $p = 0.6467$ ). The *mtx-2* cuticle (Fig. 5d, right) was significantly stiffer ( $68.7 ± 34.9$  MPa) than both WT ( $3.5 ± 2.8$  MPa,  $p < 0.0001$ ) and *gas-1* cuticles ( $15.3 ± 8.4$  MPa,  $p = 0.0008$ ), and *gas-1* significantly stiffer than WT ( $p = 0.0008$ ).

Between D2 and D8 (Fig. 5d, left), a significant 2.5-fold increase in roughness was observed in *mtx-2* worms ( $p = 0.0012$ ) while no significant differences were seen in either WT ( $p = 0.3733$ ) or *gas-1* worms ( $p = 0.2855$ ). For WT worms, this may be a combination of two factors: an increase of roughness with age due to an appearance of different non-regular structural motifs, and a decrease due to a lower height variation between annuli and

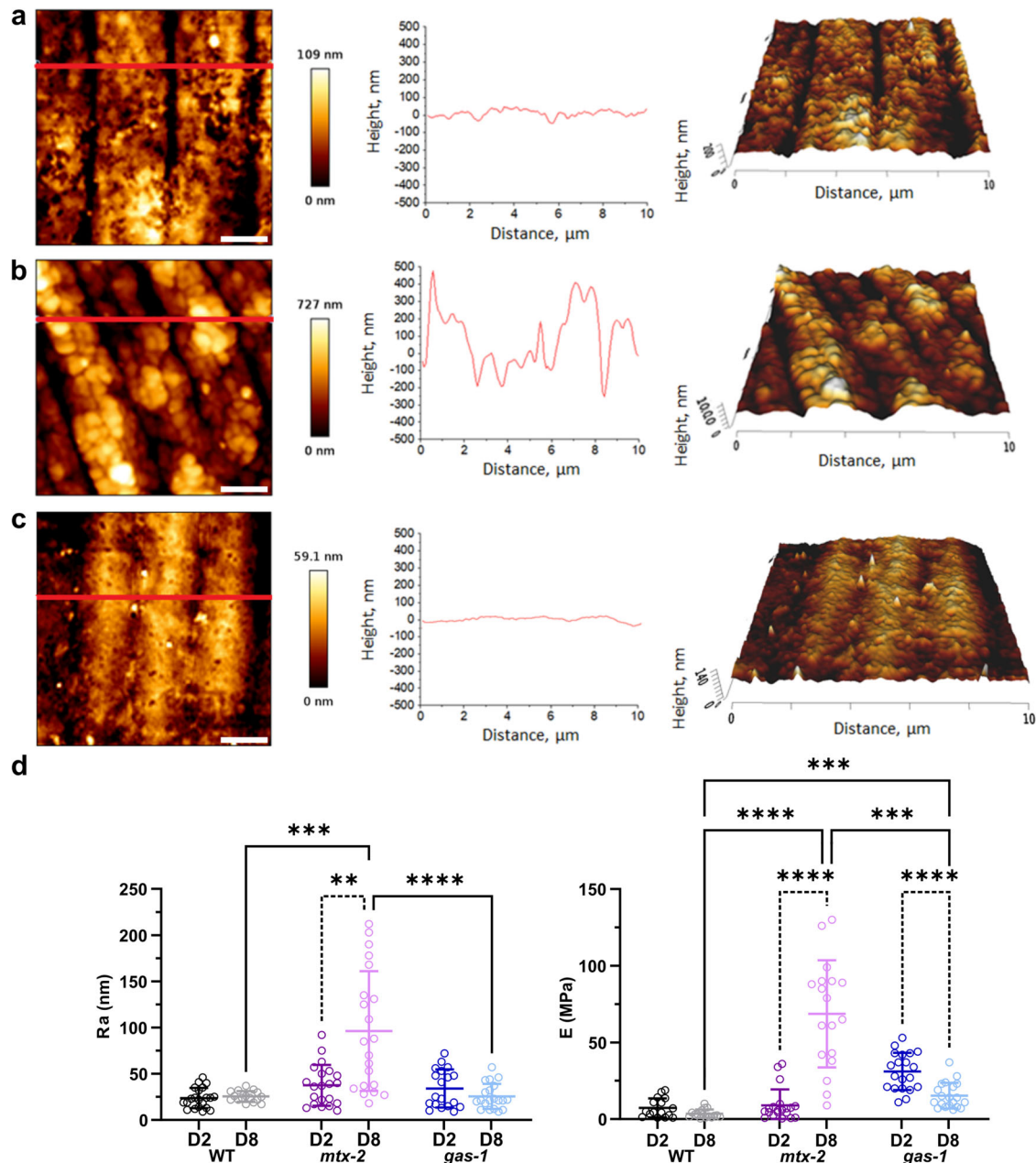


**Fig. 5 | Characterization of cuticle structure and mechanical properties of worms at D8 of adulthood by AFM and comparison with worms at D2 of adulthood.** From left to right: representative 2D topography image of a scanned tile of the cuticle surface (scale bar 2  $\mu$ m), height profile performed along the red line of the 2D topography image, and corresponding 3D topography image for a WT, b *mtx-2*, and c *gas-1* worms. d Scatter plots (mean  $\pm$  SD) of roughness ( $R_a$ , left) and elastic

modulus ( $E$ , right) of the 3 worm strains at D8 and their comparison with D2 data. The plain lines show the comparison between the 3 worm strains at D8 and the dashed lines the comparison between D2 and D8 of adulthood for the same strain (D8  $R_a$ : WT  $n = 16$ , *mtx-2*  $n = 21$ , *gas-1*  $n = 20$ ;  $E$ : WT  $n = 16$ , *mtx-2*  $n = 18$ , *gas-1*  $n = 20$ ). Statistically significant differences are shown (\*\* $p < 0.01$ , \*\*\* $p < 0.001$ , \*\*\*\* $p < 0.0001$ ).



furrows. In terms of E (Fig. 5d, right), a significant 7.5-fold increase was observed in *mtx-2* worms ( $p < 0.0001$ ), a significant decrease observed for *gas-1* mutant ( $p < 0.0001$ ), and no statistically significant difference observed in WT ( $p = 0.1163$ ). In the cuticle surface of *mtx-2* worms at D2, holes were clearly visible which were not seen at D8 (Supplementary Fig. 5). This suggests that new cuticle proteins are synthesized between D2 and D8, possibly to repair the cuticle which was not properly secreted in the early days of adulthood, which would explain the observed upregulation of a number of cuticle-related genes in *mtx-2* worms. It could also reflect a premature aging state of the cuticle since breaks and cavities have been previously observed in the cuticles of WT worms 19-days and older<sup>40</sup>.

**The cuticle of *mtx-2* worms has a disorganized wrinkled appearance**

Our SEM observations of the WT cuticle mostly showed regular, periodic arrangements of annuli separated by furrows (Fig. 6a, left), similar to those seen previously<sup>42</sup>. In contrast, the cuticles of many *mtx-2* and *gas-1* worms (Fig. 6a, middle and right, respectively) were disorganized, with obvious ultrastructural changes and an overall “crumpled” appearance. The cuticle of *mtx-2* mutant worms appeared particularly wrinkled and was similar to that seen in previous observations of *C. elegans* strains with mutations in genes which directly affect cuticle morphology<sup>43</sup>. Given the number of cuticle-related genes identified by transcriptomics in *mtx-2* worms, it’s difficult to say whether these morphological changes are due to large changes in expression of one specific gene or the synergistic effect of multiple smaller changes in expression in many genes. While the SEM observations support the AFM data, it is important to note that they have not been quantified or had statistical analyses performed on them.

***mtx-2* worms are shorter but show no difference in body width, head, or pharynx size**

Cuticle abnormalities are often associated with changes in body length<sup>44</sup> and pharynx size<sup>45</sup>. We observed that WT worms ( $804.1 \pm 114.8 \mu\text{m}$ ) were significantly longer than both *mtx-2* ( $730.1 \pm 78.4 \mu\text{m}$ ,  $p = 0.0078$ ) and *gas-1*

( $699.5 \pm 96.1 \mu\text{m}$ ,  $p = 0.0001$ ) (Fig. 6b, left) and while we found no significant difference in body thickness between *mtx-2* and WT worms ( $42.2 \pm 4.8 \mu\text{m}$  vs  $45.4 \pm 6.3 \mu\text{m}$ ,  $p = 0.0641$ ) (Fig. 6b, right), both were significantly thinner than *gas-1* worms ( $53.4 \pm 6.9 \mu\text{m}$ ,  $p < 0.0001$  and  $p < 0.0001$ , respectively). No difference was seen in pharynx length<sup>46,47</sup> (Supplementary Fig. 6) between *mtx-2* and WT worms ( $117.8 \pm 20.6 \mu\text{m}$  vs  $123.1 \pm 24.2 \mu\text{m}$ ,  $p = 0.368$ ), but *gas-1* worms had significantly shorter pharynx than both ( $107.7 \pm 17.1 \mu\text{m}$ ,  $p = 0.0177$  and  $p = 0.0011$ , respectively). The differences in pharynx size were mirrored in head size (Supplementary Fig. 6) with no difference seen between *mtx-2* and WT worms ( $152.8 \pm 22.5 \mu\text{m}$  vs  $155.1 \pm 31.1 \mu\text{m}$ ,  $p = 0.9539$ ) and both were significantly larger than *gas-1* worms ( $135.3 \pm 15.4 \mu\text{m}$ ,  $p = 0.0003$  and  $p = 0.0002$ , respectively).

**Pharyngeal pumping rate reduced and maturation delayed in *mtx-2* worms, but lifespan unaffected**

We repeated and expanded upon our previous observations of *mtx-2* worm maturation and lifespan by including *gas-1* worms, and made an assessment of pharyngeal pumping (PP) over time. PP has been shown to be a useful indicator of overall organismal health and relative age<sup>48</sup>.

The survival of 120 worms per strain taken at the L4 stage and reseeded without FUdR (5-Fluoro-2'-deoxyuridine) until death (Fig. 7a) showed no significant difference in the survival curve of *mtx-2* worms compared to WT ( $p = 0.4844$ ) and *gas-1* ( $p = 0.1036$ ), however, significant differences were observed in *gas-1* worms compared to WT ( $p = 0.0104$ ). The lifespan analysis was also performed using FUdR to prevent egg laying; no significant difference in the survival curves of WT and *mtx-2* worms cultured with FUdR was found compared to the strains cultured without FUdR ( $p = 0.4710$  and  $p = 0.6755$ , respectively), however, a significant decrease was observed for the lifespan of *gas-1* worms cultured without FUdR ( $p < 0.0001$ ) (Supplementary Fig. 7). We also confirmed previous results, showing that in the absence of FUdR, *gas-1* lifespan was shorter than WT due to its perturbed respiratory chain complex I<sup>49</sup>, and was greater than WT in the presence of FUdR<sup>50</sup>.

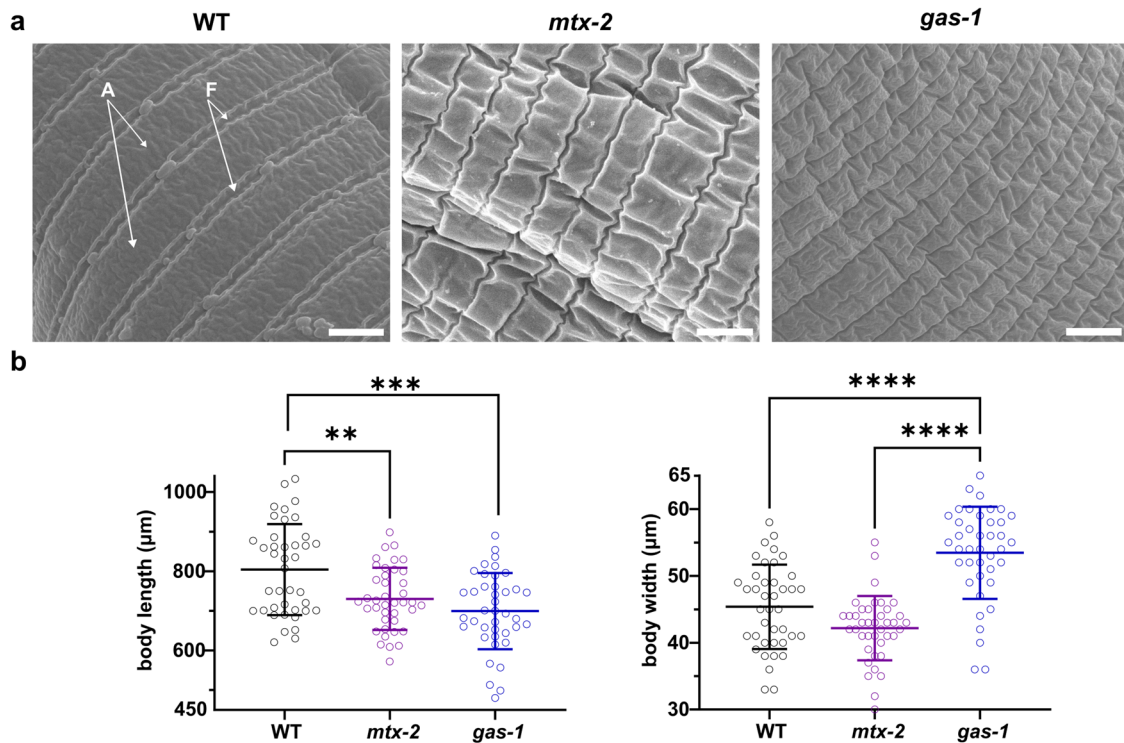


**Fig. 6 | Morphological analysis of WT, *mtx-2*, and *gas-1* worms. a** Representative SEM images of fixed L4 stage worms. Examples of annuli (A) and furrows (F) of the cuticle are indicated on the SEM image of a WT worm by white arrows (scale bars 1

μm). **b** Scatter plots (mean ± SD) of body length (left) and width (right) at D1 of adulthood ( $n = 40$ ). Statistically significant differences are shown (\*\* $p < 0.01$ , \*\*\* $p < 0.001$ , \*\*\*\* $p < 0.0001$ ).

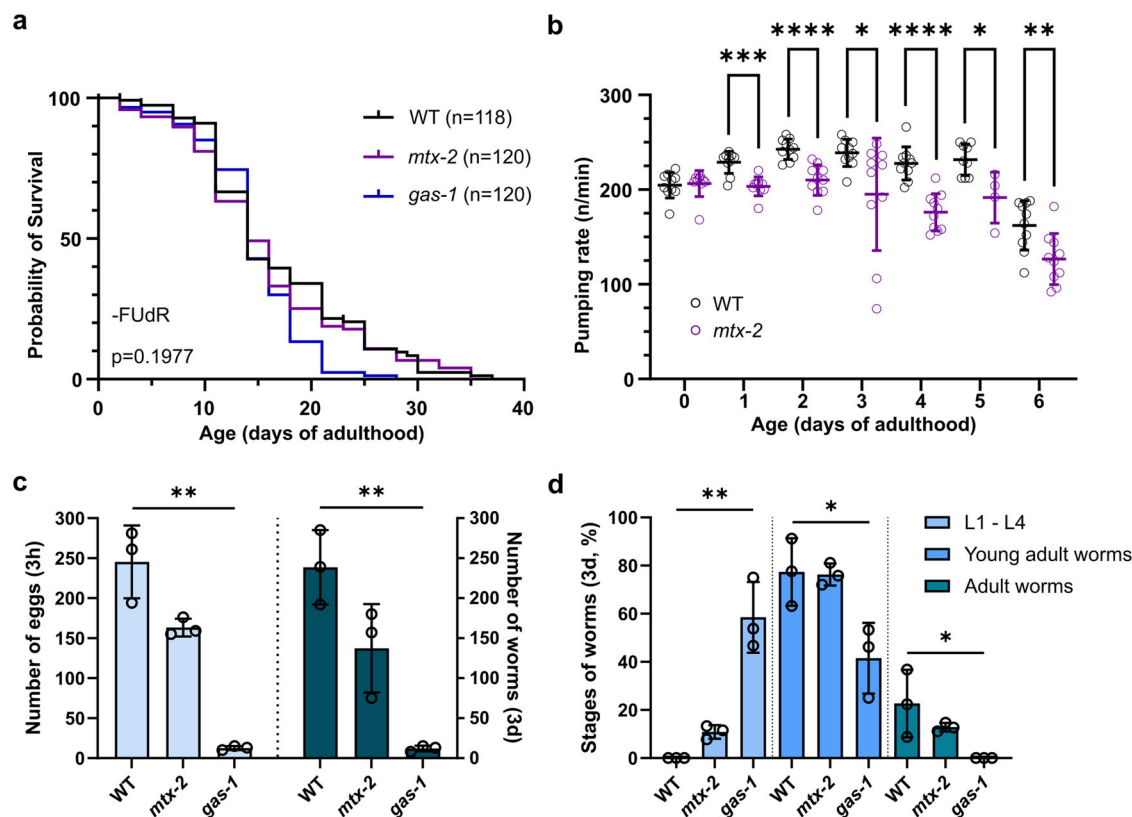


**Fig. 7 | Phenotypic characterization and comparison of worm strains.** **a** Lifespan; Kaplan-Meier survival curves (without FUdR). **b** Pharyngeal pumping (PP) in WT and *mtx-2* strains ( $n = 10$  except for D5 WT  $n = 9$  and *mtx-2*  $n = 4$ ). **c** Reproductive capacity of a total of 45 individual gravid worms per strain assessed by; number of eggs laid during 3 h (left axis) and number of worms after incubating those eggs for

3 days (right axis). **d** Developmental assay showing the percentages of worms at different stages on D1 of adulthood of WT worms. For **b**, **c**, and **d**, data are represented as mean  $\pm$  SD. For **c** and **d**,  $n = 3$  independent experiments. Statistically significant differences between different worm types are shown (\* $p < 0.05$ , \*\* $p < 0.01$ , \*\*\* $p < 0.001$ , \*\*\*\* $p < 0.0001$ ). YA: young adult.

A decline in PP, along with swimming ability and maximum movement velocity, is observed as worms age and is another indicator of overall muscle health<sup>51,52</sup>. We measured pumping frequency in worms from the L4 stage to D6 of adulthood, which corresponds to the most active period of *C. elegans*<sup>53</sup>. In WT worms (Supplementary Fig. 7), PP increased significantly from D0 to D1 ( $205 \pm 14$  n/min vs  $229 \pm 12$  n/min,  $p = 0.0188$ ), reaching a maximum at D2 ( $243 \pm 11$  n/min,  $p = 0.0001$ ), then progressively decreasing over time to a low at D6 ( $162 \pm 26$  n/min,  $p = 0.1565$ ). At D0, no difference was seen between PP in *mtx-2* and WT worms (Fig. 7b) ( $206 \pm 14$  n/min,  $p = 0.7256$ ). In contrast to WT worms, no increase in PP was seen in *mtx-2* worms over time and at each timepoint, *mtx-2* PP was significantly lower than WT. When comparing all three strains, *gas-1* PP was significantly lower than WT (Supplementary Fig. 7) on each day from D1 ( $141 \pm 26$  n/min vs  $217 \pm 18$  n/min,  $p = 0.0064$ ) to D6 ( $91 \pm 21$  n/min vs  $140 \pm 30$ ,  $p = 0.0214$ ). After D1 (*mtx-2*:  $238 \pm 78$  vs *gas-1*:  $141 \pm 26$ ,  $p = 0.0098$ ) (Supplementary Table 4), no further significant differences in PP were seen between *mtx-2* and *gas-1* from D4 to D8 of adulthood. A more detailed statistical analysis of the PP data can be found in Supplementary Tables 3 and 4.

Reproductive capacity was evaluated by the number of eggs laid by a total of 45 individual gravid worms per strain placed on NGM agar/OP50 plates for 3 h. Compared to WT, significantly fewer eggs were laid by *gas-1* worms ( $245 \pm 46$  vs  $13 \pm 3$ ,  $p = 0.0073$ , Fig. 7c, left axis). A similar trend was seen with the number of worms after 3 days of culture with significantly fewer *gas-1* worms than WT ( $12 \pm 4$  vs  $239 \pm 47$ ,  $p = 0.0073$ , Fig. 7c, right axis). These plates were then incubated for 3 days at 20°C (the average time for WT worms to reach adulthood), and developmental capacity was assessed by counting the worms at each developmental stage; larval stages (L1 - L4), young adult (YA) and adult. After 3 days, the majority of WT and *mtx-2* worms were in the YA, and *gas-1* worms were in the larval stages,

respectively (Fig. 7d). Compared to WT, significantly fewer *gas-1* worms were in the YA stage ( $77.3 \pm 14.0\%$  vs  $41.5 \pm 14.7\%$ ,  $p = 0.0369$ ), while no significant difference was observed for *mtx-2* YA worms ( $76.3 \pm 4.6\%$ ,  $p = 0.8815$ ). This means that after 3 days, the majority of WT and *mtx-2* worms are able to lay eggs and reproduce and that the majority of *gas-1* worms had not yet reached that stage of maturity. Although the differences between *mtx-2* and WT worms were not statistically significant (eggs laid:  $163 \pm 11$  vs  $245 \pm 46$ ,  $p = 0.1797$  and worms at 3 days:  $137 \pm 55$  vs  $239 \pm 47$ ,  $p = 0.1797$ ), there is a visible trend towards lower fecundity and slower development in *mtx2* worms compared to WT.

## Discussion

A commonly accepted definition of a disease model is an animal or cells which display all or some of the pathological processes that are observed in the human or animal disease. Animal models have a number of advantages over cellular models, in particular the presence of human gene orthologs, complex signaling pathways, and interplay between tissue types, all of which are critical for elucidating pathogenic mechanisms, identifying new drug targets, assessing therapeutic effect, and refining drug design. The closer a model mirrors disease pathology, the more confident we can be in extrapolating observations to humans, although valuable information can also be obtained from models designed to allow us to isolate specific aspects of a disease, even if their overall phenotype isn't strictly analogous to the human pathology<sup>54</sup>.

*C. elegans* is a well-characterized model animal which has been used to study biological processes in development, cardiology, neurobiology<sup>55</sup>, and aging<sup>56</sup> as well as diseases including Alzheimer's disease and Parkinson's disease<sup>16,57</sup>. The advantages of using worms over vertebrates include; a larger number of animals can be used per experiment (increased experimental statistical significance), shorter lifespan (more experiments in the same

timeframe), and reduced regulatory burden<sup>58</sup>. Phenotypic assays can be easily scaled up and automation is now commercially available with equipment such as the SydLab™ One<sup>59</sup>, allowing rapid, cost-effective assessment of the effects of genetic variations and response to chemical compounds, with continuous progress being made towards using *C. elegans* in true high throughput systems<sup>60</sup>.

We previously showed that *mtx-2* worms have an abnormal mitochondrial network and mitochondrial fragmentation, consistent with observations in patient-derived fibroblasts<sup>5</sup> and here we further show that multiple aspects of the *mtx-2* worm phenotype; rougher, less elastic cuticle, reduced pharyngeal pumping (a sign of aging), shorter body length, and developmental delay are analogous to clinical presentations of MADaM; skin abnormalities<sup>54</sup>, muscle degradation and dysfunction (a sign of aging), growth retardation, and developmental delay.

The mitochondrial network is dynamic, continuously undergoing biogenesis, remodeling and turnover. The subtle balance between fusion and fission maintains a healthy network of mitochondria and regulates their shape, size, number and physiological function<sup>61</sup>. A decrease in mitochondrial fusion, as observed in MADaM patient-derived fibroblasts, resulted in fission-induced mitochondrial fragmentation<sup>5</sup>. In *mtx-2* worms, the mitochondrial network is also perturbed with mitochondria significantly elongated with a swollen shape, spread, and irregular surface. The higher proportion of irregularly shaped mitochondria, suggests the fission side of the fusion/fission balance is overwhelmed which is supported by *eat-3* and *fzo-1* (mitochondrial fusion control genes) being significantly upregulated in *mtx-2* worms, whereas the expression of other notable mitochondrial fusion/fission genes (*drp-1*, *immt-1*, and *immt-2*) were not significantly affected. The elevated mitochondrial stiffness seen in *mtx-2* worm mitochondria (and in all “older” mitochondria) with AFM, may also interfere with the fission process, phagosomal engulfment, and mitophagy as it reduces membrane fluidity, preventing diffusion and insertion of membrane proteins including those belonging to molecular assemblies involved in mitochondrial interaction with other cytosolic partners; cytoskeleton, endoplasmic reticulum, nuclear membrane, and other mitochondria<sup>62</sup>.

The “tormented relief” topology of *mtx-2* worm mitochondria suggests a profound reorganization of the outer and inner mitochondrial assembly and intermembrane space. MTX-2, with its partner MTX-1, are part of the mitochondrial sorting and assembly machinery<sup>63</sup> (SAM) complex which is a binding partner of Mic60, a MICOS component involved in cristae junction (CJ) organization and maintenance<sup>63</sup>. The combination of the absence of MTX-2 and increased mitochondrial stiffness and abnormal shape and size, could modify the formation of these intermembrane spaces, affecting CJ shape and stability. The functional cooperation of electron transport chain complexes may also be affected by reorganization of intermembrane space and CJ, leading to dramatically reduced respiratory capacities and ability to adapt to changes in energy requirements. Correct insertion of all respiratory chain complexes into the inner membrane is important for their optimal molecular interplay and a “safe” electron transport. Combined with the Seahorse analysis of *mtx-2* worms showing that they exhibit the same OxPhos profile as *gas-1* worms with a non-functional mutation of a Complex-I subunit, this suggests that alteration of mitochondrial structure has impacted respiratory function.

The cytoskeleton plays a major role in maintenance of mitochondrial structure, dynamics, and regulation. It provides cells with resistance to deformation, allows shape change during movement, cargo transport, and mechanotransduction (conversion of mechanical stimuli to signaling<sup>64</sup>). In *mtx-2* worms, downregulation of ECM collagen gene expression may impact mitochondrial function-specific mechanical signals transmitted through the cytoskeleton. The prevalence of upregulated cytoskeleton genes in *mtx-2* worms identified by transcriptomics, may be related to abnormal mitochondrial morphology and function, and may influence the capacity of fission to control mitochondrial morphology<sup>65,66</sup>.

We previously observed hampered apoptosis in MADaM patient-derived cells<sup>5</sup>, leading to reduced proliferation rates and increased senescence, which may lead to a similar accumulation of unrepaired DNA lesions

and hyperactivation of a DNA repair checkpoint response seen in HGPS<sup>67</sup>. In *mtx-2* worms, nuclear DNA repair and cell cycle genes were some of the most significantly enriched DEG categories. *Cep-1* (p53) is significantly upregulated in *mtx-2* worms, and in vascular smooth muscle cells (VSMCs) increased p53 signaling leads to senescence, reduced proliferation and senescence-associated secretory phenotype and ultimately arterial calcification and stiffness, which may explain the elevated arterial disease prevalence seen in MADaM and HGPS<sup>68</sup>.

In *C. elegans*, apoptosis is mostly controlled by *ced-3*, *ced-4* (APAF1), *ced-9* (BCL2), and *egl-1*<sup>69,70</sup>. *Ced-9* is localized in mitochondria where it binds to *ced-4*. Induction of apoptosis begins when *egl-1* is expressed and binds *ced-9* leading to *ced-4* release which causes the activation of *ced-3*. *Ced-4* then rapidly translocates to the nuclear envelope (NE) in a *ced-3*-independent manner to bind to its receptor in the inner nuclear membrane, the SUN-domain protein *matefin/SUN-1*<sup>71</sup>. Since nuclear lamina structure and function are affected as well as nuclear morphology in both *mtx-2*-depleted fibroblasts and worms, perinuclear localization of *ced-4* at the inner membrane of the NE might also be affected, dramatically reducing the number of apoptotic events. In *mtx-2* worms, the observed upregulation of *ced-4* may be an attempt to compensate for the downregulation of *ced-9* expression.

The transcriptomics results align with observed altered phenotypes in *mtx-2* worms, with multiple DEGs in the *C. elegans* aging pathway and observed phenotypic markers of accelerated aging, and numerous DEGs in Wnt-signaling pathways<sup>72</sup> and observed developmental and reproductive abnormalities. It also reconfirms commonalities between progeroid syndromes as the Wnt-signaling pathway is affected in other progeroid syndromes<sup>73,74</sup>. The Wnt pathway<sup>75</sup> also plays an important role in cuticle formation<sup>27</sup> and we observed downregulation of a number of genes encoding cuticular collagen, including *bli-1*, *col-101*, and *col-176*. This partially explains both our observations of cuticle structure alteration and observations of fibroblasts from the *Lmna* Δ9 progeria mouse model where Wnt/β-catenin signaling is related to defects in expression of ECM genes<sup>76</sup>. Wnt pathway defects can affect cytoskeletal alignment and disruption of the actin networks leading to the sort of abnormal mitochondrial network distribution as well as mitochondrial shape and function that we have observed in this study and MADaM patient-derived cells. There are often interactions between pathways and the Wnt pathway has been shown to play an indirect role in the regulation of mTOR (specifically, the *let-363* gene<sup>32</sup>) which was also affected by loss of *mtx-2*.

Loss of skin elasticity and increased roughness are hallmarks of both aging and progeroid syndromes, and the combination of SEM and AFM allows us to clearly see a comparable change in cuticle morphology in *mtx-2* worms. While SEM and AFM can be considered complementary with respect to the study of surface morphology in this paper, differences exist between them which could affect observations in other applications. SEM provides better resolution, but worms must be dead and treated before analysis which may result in observation of treatment-generated artifacts. AFM resolution, while lower, is still sufficient to distinguish main surface features, and morphological and mechanical measurements can be carried out in parallel on live, untreated worms. AFM is currently underutilized in biomedical research and here we demonstrate its utility in quantifying biomechanical changes related to disease state and aging at the organismal and organelle level.

We recognise that the lack of full body rescue experiments in *mtx-2* *C. elegans* using either the *C. elegans* *mtx-2* or human MTX2 genes could be seen as a limitation of this study. That said, it should be noted that previous studies have already performed a range of rescue experiments in both MADaM patient-derived cells<sup>5</sup> and *mtx-2* K.O. *C. elegans*<sup>23</sup> and in both cases show that the mitochondrial phenotype seen in *mtx-2*-deficient cells and worms can be completely rescued. Future planned work, including tissue-specific rescue experiments, will allow us to determine the extent of rescue possible in the cuticle and whether the decrease in longevity and the developmental and reproductive delays reported here may be linked to the loss of *mtx-2* from a particular tissue/organ or its global loss.

In this study, we have expanded upon our previous characterisation of *mtx-2 C. elegans* and shown that the worm's physiological characteristics are analogous to human clinical symptoms. Through AFM, we have been able to show, for the first time, biomechanical changes in *C. elegans* cuticle and mitochondria associated with organismal aging and loss of *mtx-2*. With transcriptomics, we have uncovered a range of pathways affected by *mtx-2* loss which not only provide a better insight into the molecular mechanisms of MADaM, but also provide critical information for choosing therapeutics based on their known pathway-specific mechanism of action to test their efficacy in treating/managing MADaM. We believe we have provided ample support for the validation of *mtx2 C. elegans* as a functional model of MADaM which can be used to more clearly elucidate the molecular mechanisms of MADaM and to effectively screen potential therapeutics and treatment regimes.

## Materials and methods

The chemical reagents used in this work were purchased from Sigma-Aldrich (Merck KGaA, Darmstadt, Germany) unless otherwise stated.

### C. elegans strains

The strains used in this study, wild type (WT) Bristol N2, *gk444* (*mtx-2* k.o. with superficial WT phenotype, backcrossed three times) and *gas-1* (*fc21*) were kind gifts from CeleScreen (originally obtained from CGC, strains VC1064 and CW152, respectively). All strains were cultured at 20°C on nematode growth medium (NGM) agar plates seeded with *E. coli* OP50 in lysogeny broth (LB) (referred to as NGM agar/OP50). Unless specifically stated, prior to each experiment, worms were synchronized with a bleaching solution [0.5 N NaOH and 3% solution of sodium hypochlorite in M9 buffer<sup>77</sup> (22 mM KH<sub>2</sub>PO<sub>4</sub>, 42 mM Na<sub>2</sub>HPO<sub>4</sub>, 86 mM NaCl, 1 mM MgSO<sub>4</sub>)] and the larval stage was visually assessed under a S9E binocular stereo microscope (Leica, Wetzlar, Germany).

### Atomic Force Microscopy (AFM) characterization of C. elegans

AFM analyses of individual mitochondria and the cuticle surface of worms were performed using a NanoWizard 4 BioScience microscope (Bruker, Billerica, MA).

Calibration procedures: Prior to sample scanning, the calibration steps were performed. In particular, the deflection sensitivity was measured against the glass slide, and the spring constant was calibrated by thermal noise method. The probe radius was also calibrated as follows: firstly, CP-PNPS-SIO-D-5 cantilevers (sQube, Bickenbach, Germany), containing 10.2 µm silica bead on a cantilever with 0.32 N/m nominal spring constant, were applied to measure the elastic modulus (E) of 4% agarose gel, used as standard sample<sup>78</sup>. The deflection sensitivity and spring constant of these cantilevers were calibrated in the same way as for MLCT probes with "F" cantilevers (MLCT-F, Bruker). Three CP-PNPS-SIO-D-5 were applied to find an average value of E for agarose gel. Further, this value of E was used for MLCT-F to adjust their probe radius. Only cantilevers which required very small adjustment were finally used for measurement on *C. elegans*, in order to have all probes with rather similar radius, as the latter may have an impact on both surface roughness (through contact area between probe and sample) and elastic modulus (through applied stress and penetration depth at constant force, as the worms are not mechanically homogeneous). The use of CP-PNPS-SIO-D-5 probes was preferred as the deviation of real radius compared to nominal one is much lower for these probes compared to sharp MLCT-F.

Mitochondrial analysis: Between 100–150 WT, *mtx-2*, and *gas-1* worms at L4 stage, D2 and D8 of adulthood, were put in 5 ml of isolation buffer (IB) (210 mM mannitol, 70 mM sucrose, 0.1 mM EDTA pH 8.0, 5 mM Tris-HCl pH 7.4 and 1 mM phenylmethylsulfonyl fluoride) and kept on ice. Mitochondria were extracted using ultrasound disruption and differential centrifugation. Briefly, worms were lysed using a Vibra-Cell 75185 (60% intensity, 100 joules, three times with 2 min intervals). Then, the lysate was centrifuged at 750 g for 10 min, the supernatant was recovered and centrifuged at 12 000 g for 10 min. The supernatant was then aspirated and the

mitochondrial pellet was resuspended in 0.5 ml of IB. Prior to AFM analysis, a glass slide was coated with 0.01% poly-L-lysine solution for 20 min then rinsed with Milli-Q ultrapure water and dried under a nitrogen stream. The mitochondrial suspension was added directly to the poly-L-lysine-coated slide and incubated at RT for 15 min. The slide was then rinsed with IB to remove loosely attached mitochondria and covered with the IB prior to AFM analysis. For each condition, at least 21 individual mitochondria per worm strain were scanned using MLCT-F (with a nominal spring constant of 0.6 N/m) in Quantitative Imaging (QI) mode with the following parameters: maximum force 2 nN, oscillation amplitude 1 µm, tip velocity 200 µm/s, image resolution 128×128 px, scan size 3×3 µm<sup>2</sup>. Three independent experiments were performed. A new cantilever was used for every independent experiment (thus three cantilevers per condition). Preliminary larger size scans were performed in order to locate the mitochondria on the slide surface, and then a zoomed-in scan was performed on them. For each condition, three independent experiments were performed.

Cuticle analysis: Young adult (YA) worms (D2 of adulthood) were paralyzed in 15 g/L 2,3-butanedione monoxime in M9 buffer for 1 h, then gently transferred to a 2 mm thick 4% agarose gel and fixed in place with a topical skin glue (Dermabond™, Ethicon, Bridgewater, OH) before being immersed in M9 buffer for AFM scanning. The cuticle was analyzed using MLCT-F (with a nominal spring constant of 0.6 N/m) in QI mode. Other cantilevers present on the same side of the chip were gently broken to avoid any non-controlled contact with the worm which could potentially cause damage to it. For each condition, a minimum of 21 young or old adult (D2 or D8 of adulthood, respectively) WT, *mtx-2*, and *gas-1* worms were scanned using the following parameters: maximum force 8 nN, oscillation amplitude 1 µm, tip velocity 200 µm/s, image resolution 128×128 px, scan size 10×10 µm<sup>2</sup>. Three independent experiments were performed. A new cantilever was used for every independent experiment (thus three cantilevers per condition).

Analysis of AFM data: All data (topographical and mechanical) was processed with JPK Data processing software (Bruker, version 6.3.23). Arithmetic mean roughness (R<sub>a</sub>) was calculated across the whole height images. The Hertz model for spherical tip-sample contact was used to calculate the elastic modulus which serves as a measure of rigidity where higher E values correspond to more rigid samples<sup>79</sup>. As for the choice of Hertz model, the average maximum deformation (corresponding to maximum applied force) for different conditions was between 5 nm (*mtx-2*) and 40 nm (WT) on D8 of adulthood. As the fit for the E is done throughout the whole indentation part of approach force curve, from minimum to maximum deformation, and the nominal probe radius is 20 nm, the description of tip-sample contact as a spherical one was much more appropriate compared to conical one.

### Oxygen Consumption Rate (OCR) assessment

Respirometry profiles were determined by measuring the OCR using a Seahorse XFe96 Analyzer with the XF Cell Mito Stress Test kit and spheroid microplates (Agilent Technologies, Santa Clara, CA) as previously described<sup>31</sup> with minor modifications. Briefly, at least 15 biological replicates (6–90 animals per replicate) for each of the 3 worm strains were analyzed. Prior to OCR analysis, YA worms (at D1 of adulthood) were cultured for 24 h on NGM agar/OP50 plates with 20 mM FUDR. OCR analysis was performed according to manufacturer's instructions using 100 µM FCCP (cyanide-p-trifluoromethoxyphenylhydrazone) as an uncoupler of mitochondrial oxidative phosphorylation, then 1 mM sodium azide as a mitochondrial respiration inhibitor. Following the data treatment, first the correction against M9 buffer as negative control and then the normalization by the exact number of worms for each replicate, the OCR values were calculated for WT, *mtx-2*, and *gas-1* strains using the Seahorse Analytics application (Agilent Technologies). Respirometry profile parameters were calculated as follows: the basal respiration is the OCR before FCCP injection subtracting the non-mitochondrial respiration (after the injection of sodium azide), the maximal respiration is the OCR following FCCP and before sodium azide injection subtracting the non-mitochondrial respiration, and

the spare respiratory capacity is the difference between the maximal and basal respiration<sup>31</sup>. Three independent experiments were performed.

### Transcriptomic analysis

RNA extraction: Total RNA was extracted from approximately 300 L4 stage worms using TRIzol<sup>®</sup> (Thermo Fisher Scientific, Waltham, MA) according to the manufacturer's protocol. RNA quantification and purity assessment were performed using a NanoDrop<sup>™</sup> 2000 (Thermo Fisher Scientific). RNA samples were then frozen and stored at -80°C until use for RNA sequencing (RNA-Seq) or RT-qPCR analysis (SYBR<sup>®</sup> Green, Bio-Rad, Hercules, CA). The primers for *ama-1* and *cdc-42* were those used previously<sup>30</sup> and primers for *ugt-44*, *ced-7*, *col-12*, and *dpy-7* were designed using NCBI Primer-BLAST. The primers and the protocol used for RT-qPCR can be found in Supplementary Tables 5 and 6. Three independent RNA extractions were performed.

RNA-Seq: RNA-Seq was performed externally by the GENOM'IC core facility service of the Institut Cochin using a NextSeq<sup>™</sup> 500 System (Illumina, San Diego, CA) following an RNA quality assessment using a 2100 Bioanalyzer (Agilent Technologies). All experiments were performed using in-house protocols.

RNA-Seq data bioinformatic analysis: Initial data analysis was performed at GENOM'IC using in-house workflows. Briefly, Fastq files were aligned using STAR algorithm (version 2.7.6a), on the Ensembl release 104, *Caenorhabditis elegans* WBcel235<sup>81</sup>. Reads were counted with RSEM (v1.3.1<sup>82</sup>) and statistical analyses were performed with R Core Team<sup>83</sup> (2015, version 3.6.3) and DESeq2<sup>84</sup> (DESeq2\_1.26.0) to determine the proportion of differentially expressed genes (DEGs) between two conditions. The standard DESeq2 normalization method (DESeq2's median of ratios with the DESeq function) was used, with a pre-filter of reads and genes (reads uniquely mapped on the genome, or up to 10 different loci with a count adjustment, and genes with at least 10 reads in at least 3 different samples<sup>85</sup>). The Wald test with the contrast function and Benjamini-Hochberg FDR control procedure was used to identify DEGs (adjusted *p* value < 0.05). The R scripts and parameters used in this study are freely available on GitHub (<https://github.com/BSGenomique/genomic-rnaseq-pipeline/releases/tag/v1.0420>).

Gene Ontology (GO) enrichment analysis: Significantly DEGs were processed with WormCat<sup>33</sup> (WormCatalog). The GO terms identified three criteria: physiological function (PF), molecular function (MF), and cellular location (CL). WormCat provided a scaled bubble chart that allowed the visualization and direct comparison of complex datasets. For further understanding of molecular interaction networks, the KEGG PATHWAY Database was used.

### Scanning electron microscopy (SEM)

Approximately 200 late L4 stage worms were fixed in 2.5% glutaraldehyde overnight at 4°C. All samples were then washed in M9 buffer, postfixed in 1% osmium tetroxide for 1 h, washed in water, and dehydrated in ethanol in increasing percentage solutions from 25% to 100%. Samples were desiccated using a critical point dryer (EM CPD300, Leica), mounted on stubs with carbon tabs, coated with 20 nm gold/palladium and observed using a SEM IT700HR (JEOL, Akishima, Japan) at 5 kV with a secondary electron detector.

### Morphometric analysis

Forty live YA worms (D1 of adulthood) per strain were observed under an Eclipse H550S optical microscope (Nikon, Tokyo, Japan) and the body length, body width, pharynx and head length of each worm were measured using the NIS-Elements software, as previously described<sup>41</sup>. Three independent experiments were performed.

### Lifespan analysis

At least 30 worms of each strain in the L4 stage were placed onto separate NGM agar/OP50 plates with or without 20 mM FUdR (5-Fluoro-2'-deoxyuridine) to block egg hatching and were incubated at 20°C during 30 days.

Following the first count at day 0 (30 min after the worms seeding on the plates), the number of live/dead and lost worms per plate was counted every two days. In case worms had stopped moving, viability/mortality was confirmed by tapping the plates and gently touching worms with a platinum picker. Three independent experiments were performed.

### Pharyngeal pumping (PP)

Ten L4 stage worms per strain were placed into individual NGM agar/OP50 plates and incubated at 20°C for 6 or 8 days. Following the first measurement at day 0 (30 min after the worms seeding on the plates), the PP was measured every day for up to 6 days, or every 2 days for up to 8 days. PP was assessed by counting the number of pharyngeal contractions observed under a microscope (Axio Scope.A1, Zeiss, Oberkochen, Germany) during a 30 sec period, as previously described<sup>86</sup>. Before each measurement, worms were transferred onto new plates and PP was assessed no sooner than 10 min after transfer. For each observed worm, PP was assessed in triplicate and an average value was calculated. A worm was classified as dead if it displayed no spontaneous movement and was unresponsive after prodding with a platinum wire.

### Reproductive and developmental capacity assessment

Fifteen gravid YA worms (D1 of adulthood) from WT, *mtx-2*, and *gas-1* strains were placed onto NGM agar/OP50 plates and incubated at 20°C for 3 h. The worms were then removed and the number of eggs laid over the 3 h period was counted. These eggs were further incubated for 3 days at 20°C, the hatched worms were observed under a stereo microscope (at D1 of adulthood of WT worms), and the number of worms at each developmental stage was counted. Three independent experiments were performed and 45 worms per strain were used.

### Image processing, data plotting, statistics and reproducibility

Images obtained by optical microscopy and SEM were processed using Fiji<sup>87</sup>. The graphs and the statistical analysis presented for the AFM analyses of individual mitochondria and the cuticle surface of worms, the OCR assessment, and the phenotypic characterization of worms were performed using Prism (version 7.0, GraphPad, San Diego, CA). The normal distribution of the data was assessed using the Kolmogorov-Smirnov test. Outlier identification was performed using the Robust regression and Outlier removal (ROUT) method; in order to control the False Discovery Rate (FDR), the Q coefficient was set at 1% (FDR < 1%). The differences between two groups were evaluated using the non-parametric two-tailed Mann-Whitney test (exact *p* values) and between multiple groups using the non-parametric Kruskal-Wallis analysis of variance (ANOVA) and the uncorrected Dunn's test. The survival analysis of the 3 worm strains was based on the log-rank (Mantel-Cox) test with Bonferroni correction. The differences between the expression level of selected genes detected by RT-qPCR were evaluated using multiple t test analysis. All these analyses were conducted with the significance level at  $\alpha = 0.05$  and the differences were considered significant for \**p* < 0.05, \*\**p* < 0.01, \*\*\**p* < 0.001, \*\*\*\**p* < 0.0001. Sample sizes and number of replicates are defined in Material and Methods and in figure legends.

### Reporting summary

Further information on research design is available in the Nature Portfolio Reporting Summary linked to this article.

### Data availability

The list of significant Differentially Expressed Genes (DEGs) related to Fig. 3 is available in the Supplementary Data 1 file associated with the manuscript. The other raw data for RNA-sequencing have been deposited in the Gene Expression Omnibus (GEO), and are available at the following accession number: GSE276882. The numerical source data for the figures in the main text can be found in the Supplementary Data 2 file associated with the manuscript. All other data are available from the corresponding authors upon reasonable request.

Received: 7 November 2023; Accepted: 25 September 2024;  
Published online: 26 October 2024

## References

- Lamis, A. et al. Hutchinson-Gilford progeria syndrome: a literature review. *Cureus* **14**, e28629 (2022).
- Puente, X. S. et al. Exome sequencing and functional analysis identifies BANF1 mutation as the cause of a hereditary progeroid syndrome. *Am J Hum Genet* **88**, 650–656 (2011).
- David, A. et al. Werner syndrome: Clinical features, pathogenesis and potential therapeutic interventions. *Ageing Res Rev* **33**, 373–378 (2017).
- Gordon, L. B. et al. Association of lonafarnib treatment vs no treatment with mortality rate in patients with Hutchinson-Gilford progeria syndrome. *JAMA* **319**, 1687–1695 (2018).
- Elouej, S. et al. Loss of MTX2 causes mandibuloacral dysplasia and links mitochondrial dysfunction to altered nuclear morphology. *Nat Commun* **11**, 4589 (2020).
- Yeter Doğan, B., Günay, N., Ada, Y. & Doğan, M. E. A novel MTX2 gene splice site variant resulting in exon skipping, causing the recently described mandibuloacral dysplasia progeroid syndrome. *Am J Med Genet A* **191**, 173–182 (2023).
- Merideth, M. A. et al. Phenotype and course of Hutchinson-Gilford progeria syndrome. *N Engl J Med* **358**, 592–604 (2008).
- Olive, M. et al. Cardiovascular pathology in Hutchinson-Gilford progeria: correlation with the vascular pathology of aging. *Arterioscler Thromb Vasc Biol* **30**, 2301–2309 (2010).
- BLAST | UniProt. <https://www.uniprot.org/blast>.
- Armstrong, L. C., Saenz, A. J. & Bornstein, P. Metaxin 1 interacts with metaxin 2, a novel related protein associated with the mammalian mitochondrial outer membrane. *J Cell Biochem* **74**, 11–22 (1999).
- Armstrong, L. C., Komiya, T., Bergman, B. E., Mihara, K. & Bornstein, P. Metaxin is a component of a preprotein import complex in the outer membrane of the mammalian mitochondrion. *J Biol Chem* **272**, 6510–6518 (1997).
- Paschen, S. A. et al. Evolutionary conservation of biogenesis of beta-barrel membrane proteins. *Nature* **426**, 862–866 (2003).
- Wollweber, F., von der Malsburg, K. & van der Laan, M. Mitochondrial contact site and cristae organizing system: A central player in membrane shaping and crosstalk. *Biochim Biophys Acta Mol Cell Res* **1864**, 1481–1489 (2017).
- Kozjak-Pavlovic, V. The MICOS complex of human mitochondria. *Cell Tissue Res* **367**, 83–93 (2017).
- Alexander, A. G., Marfil, V. & Li, C. Use of *Caenorhabditis elegans* as a model to study Alzheimer's disease and other neurodegenerative diseases. *Front Genet* **5**, 279 (2014).
- Alvarez, J., Alvarez-Illera, P., Santo-Domingo, J., Fonteriz, R. I. & Montero, M. Modeling Alzheimer's Disease in *Caenorhabditis elegans*. *Biomedicines* **10**, 288 (2022).
- Bank, E. M. et al. A laminopathic mutation disrupting lamin filament assembly causes disease-like phenotypes in *Caenorhabditis elegans*. *Mol Biol Cell* **22**, 2716 (2011).
- Huelgas-Morales, G., Sanders, M., Mekonnen, G., Tsukamoto, T. & Greenstein, D. Decreased mechanotransduction prevents nuclear collapse in a *Caenorhabditis elegans* laminopathy. *Proc Natl Acad Sci* **117**, 31301–31308 (2020).
- Hsu, T. Y., Zhang, B., L'Etoile, N. D. & Juang, B. T. C. *elegans* orthologs MUT-7/CeWRN-1 of Werner syndrome protein regulate neuronal plasticity. *Elife* **10**, e62449 (2021).
- Currey, H. N. & Liachko, N. F. Evaluation of motor impairment in *C. Elegans* models of amyotrophic lateral sclerosis. *J. Vis. Exp.* <https://doi.org/10.3791/62699> (2021).
- Baskoylu, S. N. et al. Disrupted autophagy and neuronal dysfunction in *C. elegans* knockin models of FUS amyotrophic lateral sclerosis. *Cell Rep* **38**, 110195 (2022).
- Cooper, J. F. et al. Activation of the mitochondrial unfolded protein response promotes longevity and dopamine neuron survival in Parkinson's disease models. *Sci Rep* **7**, 16441 (2017).
- Zhao, Y. et al. Metaxins are core components of mitochondrial transport adaptor complexes. *Nat Commun* **12**, 1–17 (2021).
- Chen, P. X., Zhang, L., Chen, D. & Tian, Y. Mitochondrial stress and aging: Lessons from *C. elegans*. *Semin Cell Dev Biol* **154**, 69–76 (2024).
- Mack, H. I. D., Heimbucher, T. & Murphy, C. T. The nematode *Caenorhabditis elegans* as a model for aging research. *Drug Discov Today Dis Models* **27**, 3–13 (2018).
- Chisholm, A. D. & Xu, S. The *Caenorhabditis elegans* epidermis as a model skin. II: differentiation and physiological roles. *Wiley Interdiscip Rev Dev Biol* **1**, 879–902 (2012).
- Chisholm, A. D. & Hsiao, T. I. The *Caenorhabditis elegans* epidermis as a model skin. I: development, patterning, and growth. *Wiley Interdiscip Rev Dev Biol* **1**, 861–878 (2012).
- Kayser, E. B., Morgan, P. G., Hoppel, C. L. & Sedensky, M. M. Mitochondrial expression and function of GAS-1 in *Caenorhabditis elegans*. *J Biol Chem* **276**, 20551–20558 (2001).
- Layton, B. E. et al. In situ imaging of mitochondrial outer-membrane pores using atomic force microscopy. *Biotechniques* **37**, 564–573 (2004).
- Layton, B. E. & Boyd, M. B. Atomic force microscopy of isolated mitochondria. *Methods Mol Biol* **736**, 133–151 (2011).
- Koopman, M. et al. A screening-based platform for the assessment of cellular respiration in *Caenorhabditis elegans*. *Nat Protoc* **11**, 1798–1816 (2016).
- Blackwell, T.K., Sewell, A.K., Wu, Z. & Han, M. TOR signaling in *Caenorhabditis elegans* development, metabolism, and aging. *Genetics* **213**, 329–360 (2019).
- Holdorf, A. D. et al. WormCat: an online tool for annotation and visualization of *caenorhabditis elegans* Genome-Scale Data. *Genetics* **214**, 279–294 (2020).
- Fernández Casafuz, A. B., De Rossi, M. C. & Bruno, L. Mitochondrial cellular organization and shape fluctuations are differentially modulated by cytoskeletal networks. *Sci Rep* **13**, 4065 (2023).
- Solomon, T., Rajendran, M., Rostovtseva, T. & Hool, L. How cytoskeletal proteins regulate mitochondrial energetics in cell physiology and diseases. *Philos Trans R Soc B Biol Sci* **377**, 20210324 (2022).
- Raudvere, U. et al. g:Profiler: a web server for functional enrichment analysis and conversions of gene lists (2019 update). *Nucleic Acids Res* **47**, W191–W198 (2019).
- Trani, J. P. et al. Mesenchymal stem cells derived from patients with premature aging syndromes display hallmarks of physiological aging. *Life Sci Alliance* **5**, e202201501 (2022).
- Maierhofer, A. et al. Epigenetic signatures of Werner syndrome occur early in life and are distinct from normal epigenetic aging processes. *Aging Cell* **18**, 12995 (2019).
- WormBase: Nematode Information Resource. <https://wormbase.org/#012-34-5>.
- Essmann, C. L. et al. Mechanical properties measured by atomic force microscopy define health biomarkers in ageing *C. elegans*. *Nat Commun* **11**, 1–16 (2020).
- Essmann, C. L. et al. In-vivo high resolution AFM topographic imaging of *Caenorhabditis elegans* reveals previously unreported surface structures of cuticle mutants. *Nanomedicine* **13**, 183–189 (2017).
- Njom, V. S. et al. The effects of plant cysteine proteinases on the nematode cuticle. *Parasit Vectors* **14**, 1–11 (2021).
- McMahon, L., Muriel, J. M., Roberts, B., Quinn, M. & Johnstone, I. L. Two Sets of Interacting Collagens Form Functionally Distinct Substructures within a *Caenorhabditis elegans* Extracellular Matrix. *Mol Biol Cell* **14**, 1366 (2003).
- Nyaanga, J. et al. Changes in body shape implicate cuticle stretch in *C. elegans* growth control. *Cells Dev* **170**, 203780 (2022).

45. Cho, J. Y., Choi, T. W., Kim, S. H., Ahnn, J. & Lee, S. K. Morphological Characterization of small, dumpy, and long Phenotypes in *Caenorhabditis elegans*. *Mol Cells* **44**, 160 (2021).
46. Avery, L. & Shtonda, B. B. Food transport in the *C. elegans* pharynx. *J Exp Biol* **206**, 2441–2457 (2003).
47. Ferrier, A. et al. Multiple Phenotypes Resulting from a Mutagenesis Screen for Pharynx Muscle Mutations in *Caenorhabditis elegans*. *PLoS One* **6**, 26594 (2011).
48. Russell, J. C. et al. Electrophysiological measures of aging pharynx function in *C. elegans* reveal enhanced organ functionality in older, long-lived mutants. *J Gerontol A Biol Sci Med Sci* **74**, 1173 (2019).
49. Kayser, E. B., Sedensky, M. M. & Morgan, P. G. The effects of complex I function and oxidative damage on lifespan and anesthetic sensitivity in *Caenorhabditis elegans*. *Mech Ageing Dev* **125**, 455–464 (2004).
50. Van Raamsdonk, J. M. & Hekimi, S. FUDR causes a twofold increase in the lifespan of the mitochondrial mutant gas-1. *Mech Ageing Dev* **132**, 519–521 (2011).
51. Chow, D. K., Glenn, C. F., Johnston, J. L., Goldberg, I. G. & Wolkow, C. A. Sarcopenia in the *Caenorhabditis elegans* pharynx correlates with muscle contraction rate over lifespan. *Exp Gerontol* **41**, 252–260 (2006).
52. Hahm, J. H. et al. *C. elegans* maximum velocity correlates with healthspan and is maintained in worms with an insulin receptor mutation. *Nat Commun* **6**, 8919 (2015).
53. Croft, J. C., Colunga, A., Solh, L., Dillon, M. K. & Lee, T. W. Pharyngeal pumping rate does not reflect lifespan extension in *C. elegans* transgenerational longevity mutants. *MicroPubl Biol* <https://doi.org/10.17912/micropub.biology.000719> (2023).
54. Orphanet: Pigmentation anomaly of the skin. <https://www.orpha.net/en/disease/detail/79374>.
55. Pan, C. L., Peng, C. Y., Chen, C. H. & McIntire, S. Genetic analysis of age-dependent defects of the *Caenorhabditis elegans* touch receptor neurons. *Proc Natl Acad Sci* **108**, 9274–9279 (2011).
56. Yasuda, K. et al. Age-related changes of mitochondrial structure and function in *Caenorhabditis elegans*. *Mech Ageing Dev* **127**, 763–770 (2006).
57. Cooper, J. F. & Van Raamsdonk, J. M. Modeling Parkinson's Disease in *C. elegans*. *J Parkinsons Dis* **8**, 17 (2018).
58. Giunti, S., Andersen, N., Rayes, D. & De Rosa, M. J. Drug discovery: Insights from the invertebrate *Caenorhabditis elegans*. *Pharmacol Res Perspect* **9**, e00721 (2021).
59. SydLab™ one - Nagi Bioscience. <https://nagibio.ch/products-services/sydlab-system>.
60. Preez, G. D. et al. Oxygen consumption rate of *Caenorhabditis elegans* as a high-throughput endpoint of toxicity testing using the Seahorse XFe96 Extracellular Flux Analyzer. *Sci Rep* **10**, 4239 (2020).
61. Serasinghe, M. N. & Chipuk, J. E. Mitochondrial Fission in Human Diseases. *Handb Exp Pharmacol* **240**, 159–188 (2017).
62. Bach, D. et al. Mitofusin-2 determines mitochondrial network architecture and mitochondrial metabolism. A novel regulatory mechanism altered in obesity. *J Biol Chem* **278**, 17190–17197 (2003).
63. Xie, J., Marusich, M. F., Souda, P., Whitelegge, J. & Capaldi, R. A. The mitochondrial inner membrane protein mitofilin exists as a complex with SAM50, metaxins 1 and 2, coiled-coil-helix coiled-coil-helix domain-containing protein 3 and 6 and DnaJC11. *FEBS Lett* **581**, 3545–3549 (2007).
64. Fletcher, D. A. & Mullins, R. D. Cell mechanics and the cytoskeleton. *Nature* **463**, 485–492 (2010).
65. Ott, C., Dorsch, E., Fraunholz, M., Straub, S. & Kozjak-Pavlovic, V. Detailed Analysis of the Human Mitochondrial Contact Site Complex Indicate a Hierarchy of Subunits. *PLoS One* **10**, e0120213 (2015).
66. Ott, C. et al. Sam50 functions in mitochondrial intermembrane space bridging and biogenesis of respiratory complexes. *Mol Cell Biol* **32**, 1173–1188 (2012).
67. Liu, B. et al. Genomic instability in laminopathy-based premature aging. *Nat Med* **11**, 780–785 (2005).
68. Hamczyk, M. R. & Andrés, V. Vascular smooth muscle cell loss underpins the accelerated atherosclerosis in Hutchinson-Gilford progeria syndrome. *Nucleus* **10**, 28–34 (2019).
69. Del Peso, L., González, V. M. & Núñez, G. *Caenorhabditis elegans* EGL-1 disrupts the interaction of CED-9 with CED-4 and promotes CED-3 activation. *J Biol Chem* **273**, 33495–33500 (1998).
70. Tan, F. J., Fire, A. Z. & Hill, R. B. Regulation of apoptosis by *C. elegans* CED-9 in the absence of the C-terminal transmembrane domain. *Cell Death Differ* **14**, 1925–1935 (2007).
71. Penkner, A. et al. The nuclear envelope protein Matefin/SUN-1 is required for homologous pairing in *C. elegans* meiosis. *Dev Cell* **12**, 873–885 (2007).
72. Gorrepati, L. et al. Identification of Wnt Pathway Target Genes Regulating the Division and Differentiation of Larval Seam Cells and Vulval Precursor Cells in *Caenorhabditis elegans*. *G3 Genes|Genomes|Genetics* **5**, 1551–1566 (2015).
73. Choi, J. Y. et al. Diminished Canonical  $\beta$ -Catenin Signaling During Osteoblast Differentiation Contributes to Osteopenia in Progeria. *J Bone Miner Res* **33**, 2059–2070 (2018).
74. Sola-Carvajal, A. et al. Accumulation of Progerin Affects the Symmetry of Cell Division and Is Associated with Impaired Wnt Signaling and the Mislocalization of Nuclear Envelope Proteins. *J Invest Dermatol* **139**, 2272–2280.e12 (2019).
75. Jackson, B. M., Abete-Luzi, P., Krause, M. W. & Eisenmann, D. M. Use of an activated beta-catenin to identify wnt pathway target genes in *Caenorhabditis elegans*, including a subset of collagen genes expressed in late larval development. *G3 Genes|Genomes|Genetics* **4**, 733–747 (2014).
76. Hernandez, L. et al. Functional coupling between the extracellular matrix and nuclear lamina by Wnt signaling in progeria. *Dev Cell* **19**, 413–425 (2010).
77. Stiernagle, T. Maintenance of *C. elegans*. *WormBook* 1–11 <https://doi.org/10.1895/WORMBOOK.1.101.1>. (2006)
78. Kontomaris, S. V., Stylianou, A. & Malamou, A. Is It Possible to Directly Determine the Radius of a Spherical Indenter Using Force Indentation Data on Soft Samples? *Scanning* **2022**, 1–13 (2022).
79. Hertz, H. Ueber die Berührung fester elastischer Körper. *Journal für die reine und angewandte Mathematik. Band* **92**, 156–171 (2021).
80. Zhang, Y., Chen, D., Smith, M. A., Zhang, B. & Pan, X. Selection of reliable reference genes in *Caenorhabditis elegans* for analysis of nanotoxicity. *PLoS One* **7**, 31849 (2012).
81. Dobin, A. et al. STAR: ultrafast universal RNA-seq aligner. *Bioinformatics* **29**, 15–21 (2013).
82. Li, B. & Dewey, C. N. RSEM: Accurate transcript quantification from RNA-Seq data with or without a reference genome. *BMC Bioinformatics* **12**, 1–16 (2011).
83. R Core Team (2018) R A Language and Environment for Statistical Computing. R Foundation for Statistical Computing, Vienna. - References - Scientific Research Publishing. <https://www.scirp.org/reference/ReferencesPapers?ReferenceID=2342186>.
84. Love, M. I., Huber, W. & Anders, S. Moderated estimation of fold change and dispersion for RNA-seq data with DESeq2. *Genome Biol* **15**, 1–21 (2014).
85. Zhang, Y., Chen, D., Smith, M. A., Zhang, B. & Pan, X. Selection of reliable reference genes in *Caenorhabditis elegans* for analysis of nanotoxicity. *PLoS One* **7**, e31849 (2012).
86. Raizen, D., Song, B. M., Trojanowski, N. & You, Y. J. Methods for measuring pharyngeal behaviors. *WormBook* 1–13 <https://doi.org/10.1895/WORMBOOK.1.154.1> (2012).
87. Schindelin, J. et al. Fiji: an open-source platform for biological-image analysis. *Nat Methods* **9**, 676–682 (2012).

## Acknowledgements

The authors would like to thank the following; Annachiara De Sandre-Gioannoli (U1251, Marseille Medical Genetics, Aix-Marseille Université, Assistance Publique Hôpitaux de Marseille (APHM), Timone Children's Hospital, Département de Génétique Médicale et Biological Resource Center (CRB-TAC)) and Nicolas Lévy (Department of Rare Diseases, Servier, Suresnes, France) for the fruitful scientific discussions on the project, Benjamin Saintpierre (GENOM'IC core facility at the Institut Cochin) for assistance with transcriptomic analysis, Sophie Lebon, Julien Pansiot, Rachele Saleh, and Mireille Laforge (UMR 1141 INSERM NeuroDiderot) for all their assistance with OCR and RT-qPCR experiments, Sid Labdi, Clément Campillo, Guillaume Lamour and Juan Pelta (LAMBE, Université d'Evry) for their help and access support to the AFM platform, Aurélie Selvanadin and Judith Nione (Department of Pathology, Lariboisière Hospital) for their technical assistance, and Lydia Suarez and Claire Pernin (Biobank Lariboisière and Saint-Louis Hospital) for their support. Funding for this work was provided by AP-HP to P.M. and C.T-G, and equipment support was provided by the French Government Programme Investissements d'Avenir France BioImaging (FBI, N° ANR-10-INSB-04-01) and the French government (Agence Nationale de la Recherche) Investissement d'Avenir programme, Laboratoire d'Excellence "Integrative Biology of Emerging Infectious Diseases" (ANR-10-LABX-62-IBEID).

## Author contributions

C.T-G., V.A., C.L., and V.H. carried out experiments and analyzed data for the phenotypic characterization of the worms; G.S. conceived and conducted the AFM experiments and analyzed the respective data; C.P. performed the statistical analysis of the OCR assessment and the phenotypic characterization of the worms; C.S. conducted the SEM experiments; C.T-G. prepared samples for transcriptomic analysis and both C.T-G. and T.G. analyzed the transcriptomic data; C.T-G. wrote the manuscript with contributions from G.S.; C.P., G.S., T.G., C.S., P.M., S.L., H.A-B., and B.T. reviewed the original draft; C.T-G. and P.M. conceived the project; all authors read and approved the final manuscript.

## Competing interests

The authors declare no competing interests.

## Additional information

**Supplementary information** The online version contains supplementary material available at <https://doi.org/10.1038/s42003-024-06967-z>.

**Correspondence** and requests for materials should be addressed to Chloé. Talarmin-Gas or Philippe Manivet.

**Peer review information** *Communications Biology* thanks A. Stylianou, Maria De Rosa and the other, anonymous, reviewer(s) for their contribution to the peer review of this work. Primary Handling Editor: Joao Valente. A peer review file is available.

**Reprints and permissions information** is available at <http://www.nature.com/reprints>

**Publisher's note** Springer Nature remains neutral with regard to jurisdictional claims in published maps and institutional affiliations.

**Open Access** This article is licensed under a Creative Commons Attribution-NonCommercial-NoDerivatives 4.0 International License, which permits any non-commercial use, sharing, distribution and reproduction in any medium or format, as long as you give appropriate credit to the original author(s) and the source, provide a link to the Creative Commons licence, and indicate if you modified the licensed material. You do not have permission under this licence to share adapted material derived from this article or parts of it. The images or other third party material in this article are included in the article's Creative Commons licence, unless indicated otherwise in a credit line to the material. If material is not included in the article's Creative Commons licence and your intended use is not permitted by statutory regulation or exceeds the permitted use, you will need to obtain permission directly from the copyright holder. To view a copy of this licence, visit <http://creativecommons.org/licenses/by-nc-nd/4.0/>.

© The Author(s) 2024